



# Vertical-axis rotation in East Kopet Dagh, NE Iran, inferred from paleomagnetic data: oroclinal bending or complex local folding kinematics?

Jonas B. Ruh<sup>1,2</sup>  · Luis Valero<sup>1,3</sup> · Lotfollah Aghajari<sup>4</sup> · Elisabet Beamud<sup>5</sup> · Gholamreza Gharabeigli<sup>4</sup>

Received: 22 June 2019 / Accepted: 10 September 2019 / Published online: 25 September 2019  
© Swiss Geological Society 2019

## Abstract

The Kopet Dagh Mountains in NE Iran result from Cenozoic tectonic inversion of Triassic and Jurassic rifts that formed along the southern margin of the Eurasian continental plate. The Kopet Dagh defines an arcuate orogen leading to the suggestion that oroclinal bending took place during its formation. We performed a paleomagnetic study including seven sampling sites of Paleocene formations around the Kalat syncline in the East Kopet Dagh to test whether this part of the mountain belt experienced vertical-axis rotation. Paleomagnetic measurements and a reversals test indicate that parts of the collected samples may have been partially remagnetized. Overall paleomagnetic directions of all sample sites show a mean declination of  $12.5^\circ$ , which is the expected direction for stable Europe in the Paleocene and therefore negates any rotation related to regional tectonic events. Directions calculated only from reversely polarized paleomagnetic data, however, suggest clockwise vertical-axis rotations up to  $21^\circ$  since the Paleocene. Numerical modelling of a viscous multi-layer folding mimicking the Kalat syncline stratigraphy suggests that local deviations in overprinted site-mean directions and orientation of the maximum axes of the AMS ellipsoid may be related to complex folding kinematics, acquired after regional vertical-axis rotation, where related viscous flow of relatively weak interlayer is represented by the sampled Paleocene formation.

**Keywords** Paleomagnetism · Kopet Dagh Mountains · Numerical modelling · Vertical-axis rotation · Arabia-Eurasia collision

---

Editorial handling: S. Schmid.

---

**Electronic supplementary material** The online version of this article (<https://doi.org/10.1007/s00015-019-00348-z>) contains supplementary material, which is available to authorized users.

---

✉ Jonas B. Ruh  
jonas.ruh@erdw.ethz.ch

- <sup>1</sup> Institute of Earth Science Jaume Almera, ICTJA, CSIC, Barcelona, Spain
- <sup>2</sup> Geological Institute, ETH Zürich, Zürich, Switzerland
- <sup>3</sup> Department of Geology, Autonomous University of Barcelona, Bellaterra, Spain
- <sup>4</sup> National Iranian Oil Company, Tehran, Iran
- <sup>5</sup> University of Barcelona, Paleomagnetic Laboratory CCiTUB at ICTJA, CSIC, Barcelona, Spain

## 1 Introduction

The Kopet Dagh mountain belt is situated in northeast Iran and extends for over  $\sim 700$  km from Afghanistan in the East to the South Caspian Basin in the West along the border to Turkmenistan (Fig. 1). The Kopet Dagh is an intracontinental orogen representing the tectonic boundary between Eurasia and the Central Iranian Block (Robert et al. 2014). The mountain range results from tectonic inversion of a rift basin that underwent extension during the middle Jurassic (Kavoosi et al. 2009), potentially as a back-arc basin to the Neotethys subduction zone (today the Zagros mountains; Fig. 1) further to the south (Brunet et al. 2003; Zanchi et al. 2006). The initiation of uplift, i.e. tectonic inversion, of the Kopet Dagh mountains took place during the Cenozoic, when closure of the Neotethys led to the formation of the Zagros orogen and the Iranian continental blocks were pushed northward together with the Arabian plate (Golonka 2004; Lyberis and Manby 1999).

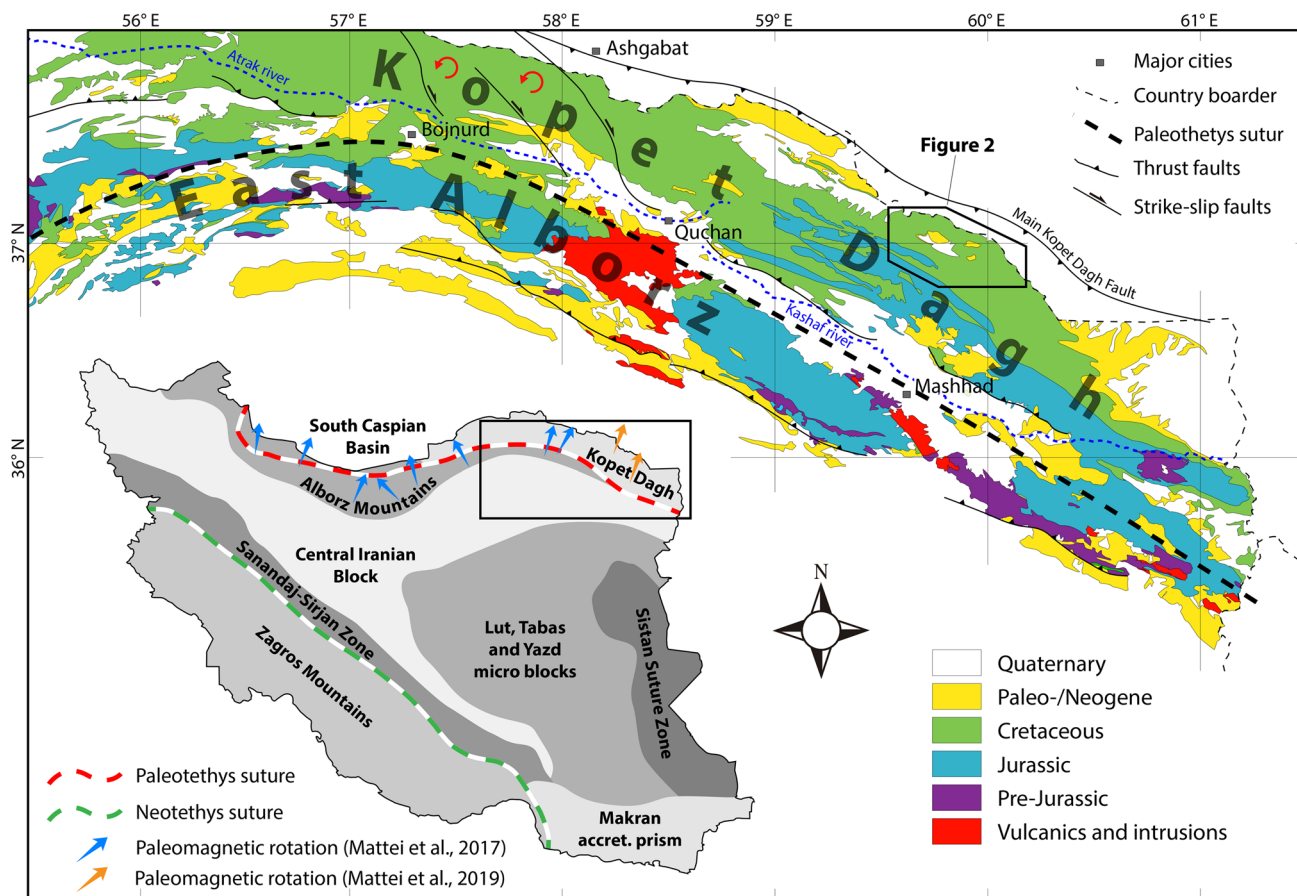


**Fig. 1** Colored upper part shows the geological map of the Kopet Dagh and the East Alborz (modified after Afshar 1982, 1983; Afshar et al. 1984; Afshar Harb et al. 1986; Behrouzi et al. 1993; Bolourchi et al. 1987; Eftekhari-Nezhad et al. 1992; Jalilian et al. 1992; Tatavousian et al. 1993). Red circled arrows indicate local vertical-axis rotation (Hollingsworth et al. 2010). Black rectangle shows

location of Fig. 2. Gray-scaled lower left part shows Iran and its tectonic blocks and major sutures. Blue and orange arrows indicate paleomagnetic directions from Mattei et al. (2017; 2019) related to oroclinal bending of the Alborz. Black square indicates location of the colored map above

However, the exact onset of uplift is still a matter of debate (Robert et al. 2014). Lyberis and Manby (1999) propose that rift inversion occurred during the late Miocene, whereas most studies advocate that the Kopet Dagh began to grow already  $\sim 30$  Ma ago (Berberian and King 1981; Golonka 2004; Hollingsworth et al. 2010), similar to the uplift of the Alborz mountains (Ballato et al. 2015; Rezaeian et al. 2012). In either case, the  $\sim 75$  km of shortening in the Kopet Dagh (Lyberis and Manby 1999) has mainly been accommodated by reactivation of inherited rift faults within the basement, resulting in thrusting and fault-propagation folding of the overlying strata (Robert et al. 2014; Ruh and Vergés 2018).

At present, northeastern Iran accommodates ca. 4–11 mm/a of the convergence between Arabia and Eurasia (Reilinger et al. 2006; Vernant et al. 2004). In the western part of the Kopet Dagh, shortening takes place along thrusts and minor left-lateral strike-slip faults, whereas right-lateral strike-slip faults dominate recent

deformation in the central part of the mountain range (e.g., between Bojnurd and Quchan; Fig. 1), according to GPS data and earthquake focal mechanisms (Hollingsworth et al. 2006, 2010; Tavakoli 2007). This strike-slip motion in the western and central part of the mountain range reportedly initiated between  $\sim 10$  Ma (Hollingsworth et al. 2008) to  $\sim 5$  Ma (Shabanian et al. 2012) and has been related to vertical block faulting and rotation. In the eastern Kopet Dagh, shortening occurs on major basement-involved thrust faults (Hollingsworth et al. 2010; Robert et al. 2014).

In contrast to local block rotation related to strike-slip faults, regional vertical-axis rotation of the western and eastern Kopet Dagh has been proposed to have taken place as a result of oroclinal bending (Hollingsworth et al. 2010; Mattei et al. 2017; 2019). Hollingsworth et al. (2010) advocate that the Alborz and Kopet Dagh mountains have initially been linearly E–W-trending and that oroclinal bending started contemporaneously with the uplift of the

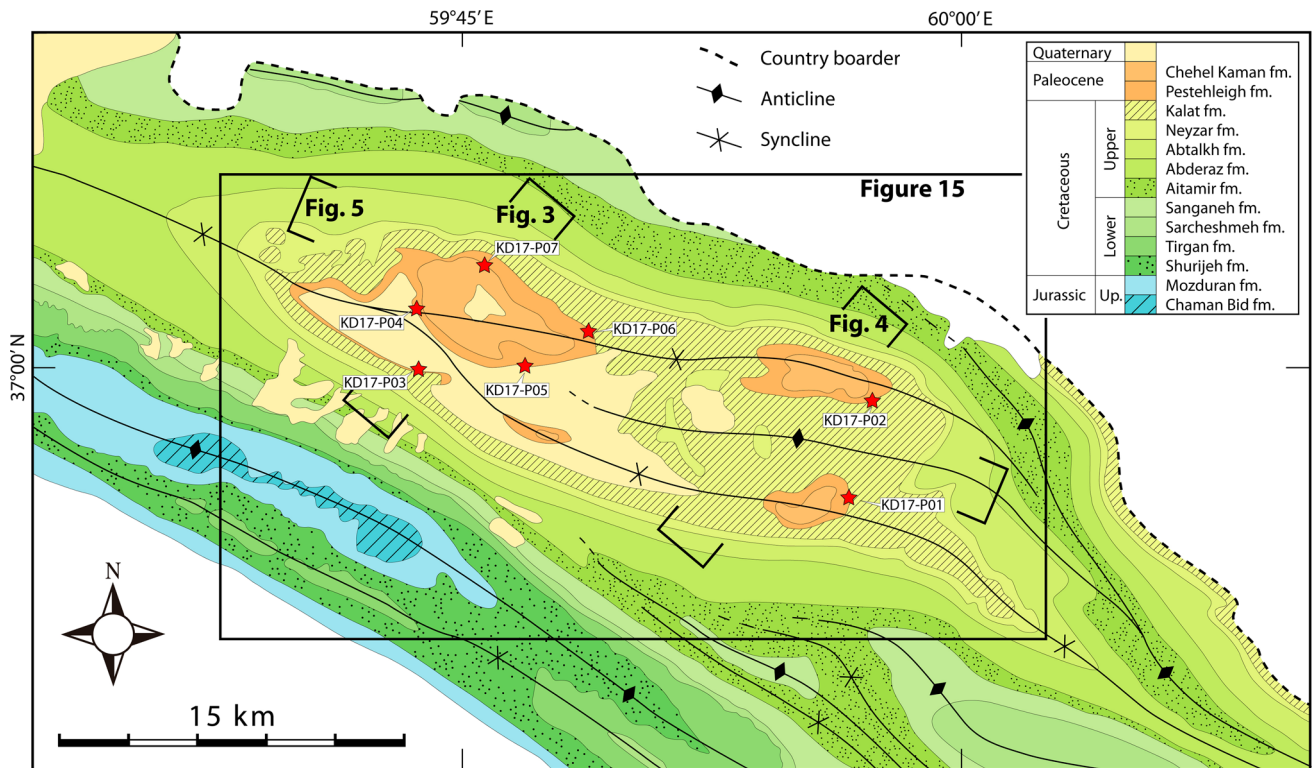


**Fig. 2** Geological map with most important structural features and stratigraphic description of the Kalat syncline. Locations of sample sites P01–P07 are indicated as red stars. Approximate location of seismic profiles of Figs. 3, 4 and 5 and the map of Fig. 15 are shown as black outlines

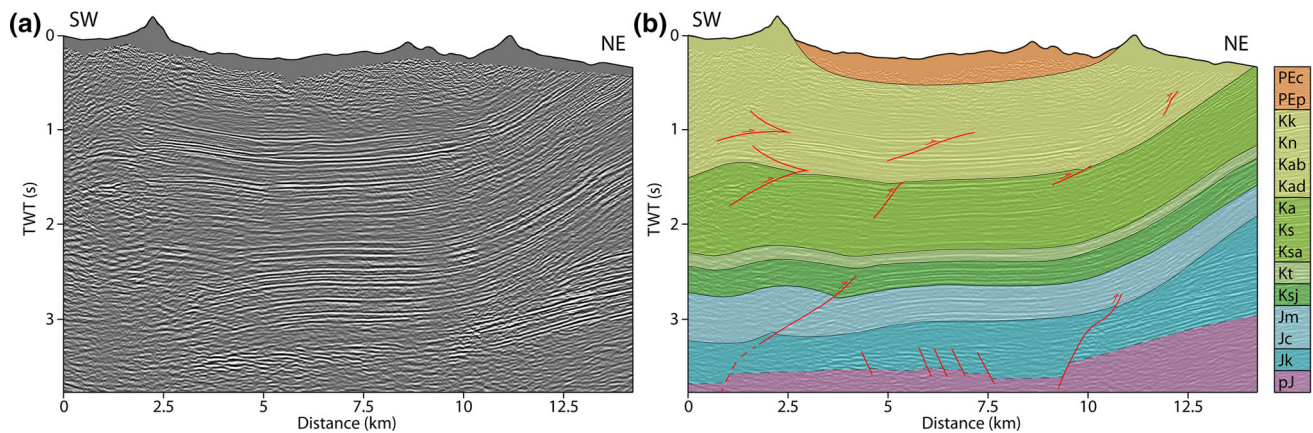


**Fig. 3** Seismic section (a) and its interpretation (b) of a section cross-cutting the Kalat syncline in the west. See Fig. 2 for approximate location. Two minor north-verging thrusts in Jurassic strata root down into basement structures. In this and the subsequent figures: *pJ* pre-Jurassic, *Jk* Kashafrud Formation (Middle Jurassic), *Jc* Chaman Bid Formation (Upper Jurassic), *Jm* Mozduran Formation (Upper Jurassic); Shurijeh Formation (Lowermost Cretaceous), *Kt* Tirgan

Formation (Barremian), *Ksa* Sarchashmeh Formation (Aptian), *Ks* Sanganeh Formation (Albian), *Ka* Aitamir Formation (Cenomanian), *Kad* Abderaz Formation (Upper Cretaceous), *Kab* Abtalkh Formation (Campanian), *Kn* Neyzar Formation (Campanian), *Kk* Kalat Formation (Campanian–Maastrichtian), *PEp* Pestehleigh Formation (Lower Paleocene), *PEc* Chehel Kaman Formation (Upper Paleocene)

Kopet Dagh range  $\sim 30$  Ma ago, due to the indentation of the South Caspian rigid block into northern Iran (Allen et al. 2003). Paleomagnetic measurements throughout the Alborz indicate that progressive vertical-axis rotation of an initially linear mountain belt has formed the present-day curvature before late-middle Miocene (Fig. 1; Cifelli et al.

2015; Mattei et al. 2017; 2019). With respect to the Kopet Dagh, the proposed oroclinal bending would result in clockwise vertical-axis rotation in the east and anti-clockwise vertical-axis rotation in the west (Hollingsworth et al. 2010).

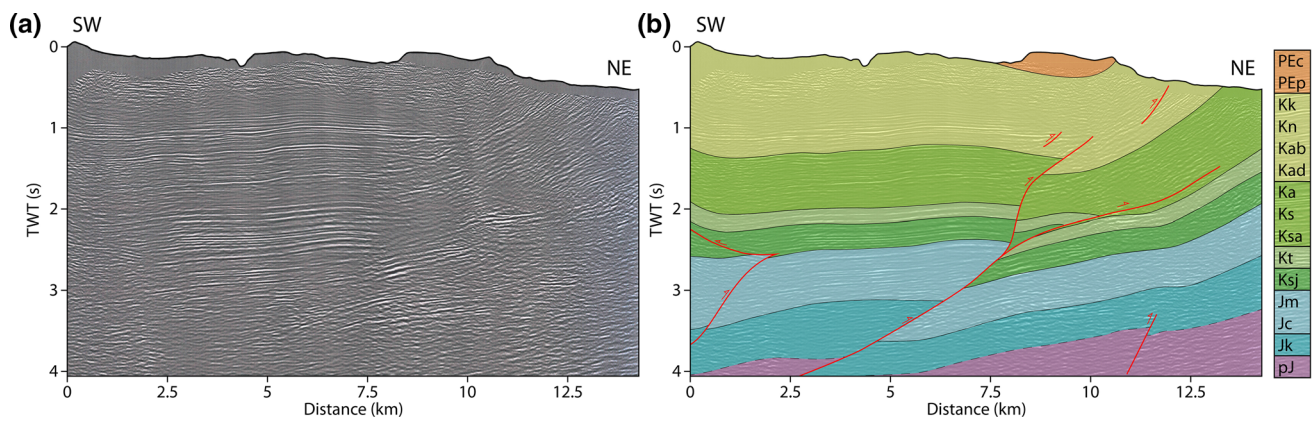


**Fig. 4** Seismic section (a) and its interpretation (b) of a section crossing the Kalat syncline in the east. See Fig. 2 for approximate location. North-verging rooting down to the basement cuts the section

up to Upper Cretaceous strata. A lower splay of the thrust branches into the Lower Cretaceous that acts as a layer parallel detachment

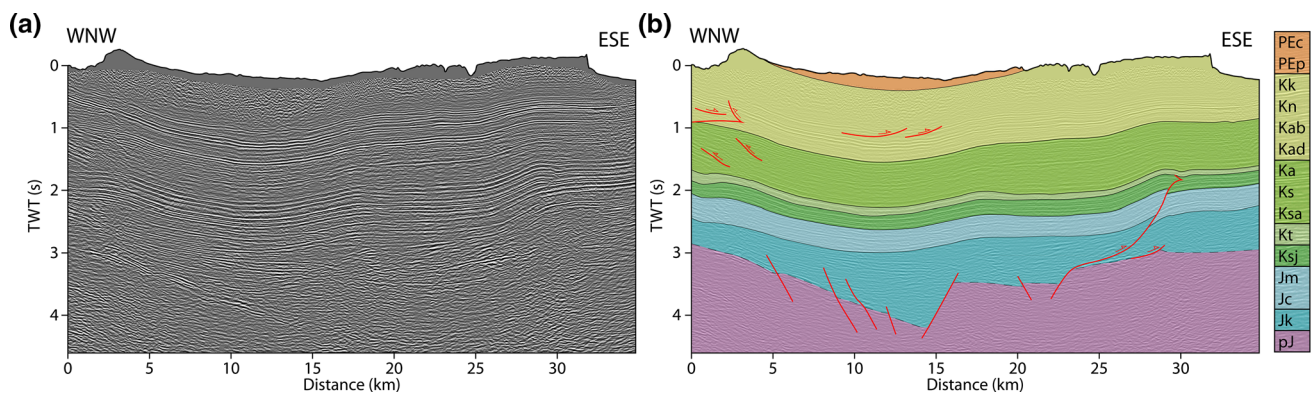


**Fig. 5** Seismic section (a) and its interpretation (b) of a section cutting parallel to the main Kalat syncline strike. See Fig. 2 for approximate location. Several basement-related normal faults appear

in pre-Jurassic rocks. ESE-verging thrust rooting down into a basement normal fault. Minor offsets occur in Upper Cretaceous strata

Paleomagnetism has proven to be a viable tool to measure vertical-axis block rotations in mountain belts (e.g., Lowrie and Hirt 1986; Schwartz and Van der Voo 1983; Sussman et al. 2004). Whereas a wealth of paleomagnetic studies have been conducted to obtain vertical-axis rotation in the Alborz mountains (Cifelli et al. 2015, 2016; Mattei et al. 2015, 2017), there is only little data available from the Kopet Dagh range (Bazhenov 1987). Here, we present results of paleomagnetic measurements from several sites around the Kalat syncline along the northern mountain front of the East Kopet Dagh (Figs. 1, 2) in order to test the above-mentioned proposition of vertical-axis block rotation. Paleomagnetic directions and magnetic fabric determined from anisotropy of magnetic susceptibility (AMS) measurements are discussed to describe the effect of three-dimensional folding kinematics on local vertical-axis rotation (e.g., Smith et al. 2005). Furthermore, we present a simple three-dimensional numerical experiment to better understand the folding kinematics, in particular local rotations in the horizontal

plane, of a doubly-plunging syncline and discuss the model outcome with respect to the paleomagnetic data.

## 2 Structure and stratigraphy of the Kalat syncline

The Kalat syncline lies in the northwestern part of the Kopet Dagh mountains along the Iran–Turkmenistan border (Fig. 1). It is situated  $\sim 100$  km east of major strike-slip faults that crosscut the entire mountain range and is therefore not affected by local rigid block rotation related to those lateral motions (Fig. 1). The Kalat syncline forms an elongated structure striking parallel to the Main Kopet Dagh Fault, which marks the northeastern boundary of the orogeny and represents a major inherited basement structure reactivating Paleozoic normal faults (Amurskiy 1971; Maggi et al. 2000; Robert et al. 2014). The western part of the syncline is flanked by two parallel striking anticlines to the SSW and the NNE, whereas deformation gets

partitioned into laterally overlapping folds forming relay structures to the east (Fig. 2). The main fold axis of the Kalat syncline plunges inward at very shallow angles (see Table 1) resulting in a slightly conical appearance.

The stratigraphic column cropping out around the Kalat syncline includes Upper Jurassic to Paleocene rocks, excluding the Quaternary cover (Fig. 2). The following lithological descriptions are a summary of the more detailed investigation of Robert et al. (2014) and references therein. The oldest rocks in the area are formed by Late Jurassic alterations of shale and marly limestones (Chaman Bid Formation) and well-bedded limestone to siliciclastic deposits (Mozduran Formation) and appear within the hinge of the anticline towards the SW. Towards the north, and the center of the Kalat syncline, the stratigraphy is entirely conserved. Jurassic rocks are overlain by nine Cretaceous formations, with the lowest one consisting of red siliciclastic sandstones and gypsum/anhydrite deposits (Suriyeh Formation) followed by marls and orbitolinid-rich limestones (Tirgan Formation). The upper part of the Lower Cretaceous consists of gray marls, shale and limestones (Sarcheshmeh Formation) and inter-layered marls and sandstones (Sanganeh Formation). The Upper Cretaceous begins with mudstones and minor (partially glauconitic) sandstones (Aitamir Formation) overlain by calcareous and marly shales (Abderaz Formation) and calcareous shales, limestones and small rudist-patch reefs (Abtalkh Formation). The uppermost Cretaceous consists of glauconite deposits, clays and minor sandstones (Neyzar Formation) progressively transitioning into bioclastic limestone and carbonate build-ups (Kalat Formation). Paleocene deposits crop out in the hinge of the Kalat syncline and consist of red continental silt- and sandstones and minor conglomerates (Pestehleigh Formation) and overlying white carbonates (Chehel Kaman Formation). The stratigraphic succession indicates shallow marine to continental environments with two main hiatuses and local erosion located at the top of the Aitamir and Kalat formations.

In the following paragraphs, the deeper structure of the Kalat syncline is described by interpreting three seismic sections (Fig. 3, 4, 5). Seismic data has been processed at the National Iranian Oil Company (NIOC). Their interpretation is based on surface geology, boreholes and cross-correlation with other seismic profiles from the region. Two sections crosscut the fold in a perpendicular manner from SW to NE and one along strike from WNW to ESE (see Fig. 2 for location). All seismic sections reach down to undifferentiated pre-Jurassic basement (pJ) and its contact to the overlying Middle Jurassic Kashafud Formation (Jk), which was deposited in a rift system (see also Robert et al. 2014) succeeding the Cimmerian orogeny (Wilmsen et al. 2009). Seismic data of the western section

**Table 1** Paleomagnetic data from the Kalat syncline

Location	Site	Latitude (°N)	Longitude (°E)	Formation	Lithology	Bedding	N/n	BTC				ATC			
								D (°)	I (°)	k (-)	$\alpha95$ (°)	D (°)	I (°)	k (-)	$\alpha95$ (°)
	KD17-01	36°55'49.11"	59°55'39.90"	Pestehleigh	Red siltstone	258/03	14/7	29.6	36.3	6.06	26.7	27.9	38.2	6.06	26.7
	KD17-02	36°58'48.87"	59°57'9.22"	Pestehleigh	Red siltstone	014/14	16/9	11.4	52.9	5.38	24.5	12	38.9	5.39	24.5
	KD17-03	37°0'0.01"	59°43'27.13"	Pestehleigh	Red siltstone	050/17	13/11	347.4	53.6	21.64	10	2.4	44.4	21.9	10
	KD17-04	37°1'44.12"	59°44'14.76"	Pestehleigh	Red siltstone	085/06	9/4	14	49.6	10.83	29.3	20.3	47.3	10.82	29.3
	KD17-05	36°59'41.53"	59°46'51.68"	Pestehleigh	Red siltstone	030/27	14/13	2.8	51.1	32.11	7.4	11.4	26.1	32.05	7.4
	KD17-06	37°0'57.72"	59°48'39.34"	Pestehleigh	Red siltstone	216/02	11/2	329	58.3	57.54	33.5	325.9	59	57.66	33.5
	KD17-07	37°3'2.34"	59°45'45.94"	Chehel Kaman	Carbonate	210/29	11/2	8.7	34.4	6.03	135.8	353	60.1	6.05	135.3

and its interpretation illustrate an open syncline with a wavelength of  $\sim 15$  km (Fig. 3). Small rift-related faults are observed within the pre-Jurassic basement reaching into the syn-rift Jurassic Kashafrud Formation (Fig. 3). The small offset shown by those faults and the smooth contact between Middle to Upper Jurassic strata indicates little to no fault reactivation during Cenozoic shortening. However, several thrusts can be interpreted within the folded strata, all verging towards the NE (Fig. 3). The most prominent are cutting the Middle Jurassic in the SW resulting in a minor fault-bend fold and two fish-tail structures in the Cretaceous strata, probably branching into potential detachment horizons, as suggested by Robert et al. (2014).

In the east of the syncline, the interpretation of a  $\sim 14$  km long seismic profile suggests major implication of northeast-verging thrust faults (Fig. 4). Fault-related deformation includes a shallow angle thrust fault cutting through most parts of the stratigraphic sequence, including the pre-Jurassic basement, branching into a Lower Cretaceous layer-parallel detachment. A splay of this fault crosscuts the Lower Cretaceous strata and branches into Upper Cretaceous formations (Fig. 4). Furthermore, thrusting of the pre-Jurassic units and related fault-propagation folding of the overlaying Jurassic strata indicate normal fault reactivation within the basement. On the surface, the resulting structure appears as two synclines, with hinges at  $\sim 1$  km and  $\sim 10$  km in the seismic section, and a central anticline at  $\sim 6$  km (Fig. 4), as illustrated in the geological map (Fig. 2).

The seismic profile parallel to the main strike of the orogen cuts the Kalat syncline along  $\sim 35$  km direction WNW–ESE (Fig. 5). The interpretation of this seismic section illustrates an open syncline with shallow-dipping limbs. The contact of the Kalat and the Pestehleigh formations plunges inward at an angle  $< 5^\circ$ , taken into account the vertical exaggeration. Some compressional structures such as an east-verging thrust cutting Jurassic and Lower Cretaceous strata in the east and a fish-tail structure and some small thrusts in the Cretaceous in the west are observed (Fig. 5). A steeply-dipping offset within the pre-Jurassic basement forming a typical half-graben suggests the occurrence of N–S trending rift structures below the Kalat syncline (e.g., Brunet et al. 2017; Khain et al. 1991). The hinge zone of the Kalat syncline is located above the basement-related half-graben structure, where the contact between pre-Jurassic to Jurassic units is deepest (Fig. 5). However, whether basement faults have been reactivated during the Cenozoic growth of the mountain range cannot be confirmed from the seismic profile. Potentially, inherited normal faults triggered localization of deformation during folding.

## 3 Methodology

### 3.1 Sampling

In order to obtain vertical-axis rotation of the Kalat syncline related to the uplift of the Kopet Dag, paleomagnetic samples have to be collected from stratigraphic units older than Oligocene, the earliest suggested timing for the initiation of shortening in NE Iran (Hollingsworth et al. 2010). We collected a total of 93 sample cores from six sites situated in the Paleocene Pestehleigh Formation, which contains reddish continental sediments, and one site from the overlaying Chehel Kaman Formation, which consists of white carbonates (Fig. 2; Table 1). In the Pestehleigh Formation, sampling was restricted to the fine-grained components, i.e. clays and siltstones. Sampling sites have been chosen to cover different parts of the syncline, including both limbs and the hinge zone, the western and the eastern part (Fig. 2).

### 3.2 Magnetic measurements

Initially, the natural remanent magnetization (NRM) of every sample was measured before stepwise demagnetization due to heating or an induced alternating field (AF). NRM and magnetization were measured after every demagnetization step using a 2G Enterprise 755R, three-axis DC superconducting quantum interference device (SQUID) rock magnetometer (background magnetic moment around  $10^{-9}$  emu/cc) at the Paleomagnetic Laboratory at the ICTJA–CSIC in Barcelona. One specimen of every core (93 samples) has been stepwise demagnetized thermally in 18 steps up to a maximum of 670 °C. Samples were both heated and cooled for at least 45–60 min, respectively, with an ASC TD48 oven with an internal field of less than 10 nT. Additionally, AF demagnetization was applied to 35 samples using a ASC D-Tech 2000 AF demagnetizer. AF demagnetization was obtained by 18 steps up to an alternating field of 200 mT. Furthermore, 10 of the AF demagnetized samples were further thermally demagnetized until complete loss of magnetization.

Demagnetization curves were illustrated with vector end point diagrams to obtain different magnetic components depending on temperature or AF intensity (Zijderveld 1967). The orientation of different magnetization components was identified by using the Remasoft software (Chadima and Hroudá 2006), where line fitting of principal components is achieved with the method of Kirschvink (1980) and mean directions of the characteristic components at site level are calculated by the method of Fisher (1953).

A cross-component isothermal remanent magnetization (IRM) was induced on three samples (P01b, P05c, P07e) and thermally demagnetized to identify the mineralogy of the magnetic carrier by relating unblocking temperatures and coercivities of specific ferromagnetic minerals (Lowrie 1990). IRM was induced by a ASC impulse magnetizer IM10-30 along three orthogonal directions in successively smaller fields of 1.2 T ( $z$ -axis), 0.3 T ( $y$ -axis) and 0.1 T ( $x$ -axis). Thermal demagnetization was carried out with a Schönstedt TSD-1 thermal demagnetizer and the intensity was measured with a spinner magnetometer JR6A (Agico).

### 3.3 AMS measurements

Anisotropy of low-field magnetic susceptibility (AMS) measurements allows recognizing the average preferred orientation of particles within a sample and can be used to infer tectonic fabric in weakly deformed rocks (Borradaile and Henry 1997). The orientation and values of the three principle axes of the AMS ellipsoid are achieved by measuring the susceptibility, i.e. the potential of magnetization in response to an applied field, along 15 different directions of the sample (Jelinek 1981). The shape of the AMS ellipsoid results from both magnetic and physical properties of all grains within a rock sample (Hrouda 1982; Uyeda et al. 1963) and indicates whether the magnetic fabric is sedimentary or overprinted due to layer parallel shortening (Weil and Yonkee 2009; Fig. 6): During sediment accumulation, the minimum axis of the AMS ellipsoid is vertically oriented with the maximum and intermediate AMS principal axes randomly distributed in the horizontal plane (stage A). Initial tectonic overprint is characterized by the maximum principal axis aligning perpendicular to the shortening direction (stage B). With further shortening, the minimal principal axis of the AMS ellipsoid rotates in a vertical plane (stage C) towards being parallel with the shortening direction (stage D). The fully

overprinted tectonic fabric of the AMS ellipsoid shows a minimum axis parallel to shortening and a vertically oriented maximum axis (stage E). AMS of each sample was measured before demagnetization with an AGICO Kappabridge KLY-2 susceptibility bridge with an operating frequency of 920 Hz and a sensitivity of  $4.10^{-08}$  for a specimen of nominal volume of 10 cc. AMS results are illustrated with the Anisoft software (Chadima et al. 2018).

## 4 Rock-magnetic results

The majority of measured samples show intensities of the NRM between  $2 \times 10^{-4}$  and  $3 \times 10^{-2}$  A/m (Fig. 7). White carbonate samples from the Chehel Kaman Formation (site P07) exhibit relatively low intensities in contrast to samples from the red beds of the Pestehleigh Formation (sites P01–06). Values of initial magnetic susceptibility (before thermal or AF demagnetization) corrected for sample volume range between  $3 \times 10^{-5}$  and  $3 \times 10^{-4}$  [SI] (Fig. 7). Similar to intensity, carbonate samples show the lowest observed susceptibilities. The ratio of NRM intensity to magnetic susceptibility (normalized intensity in A/m) can provide a first-order indication of magnetic mineralogy variations. Most measured samples plot within a normalized intensity range of 5–20 A/m (Fig. 7), suggesting that there is no major change in magnetic carrier for the different sample sites.

Three-component IRM demagnetization measurements on three selected samples have been conducted allowing for a better interpretation of the ferromagnetic mineral content (Fig. 8; Lowrie 1990). In general, the thermally distributed intensity decay observed in all samples may obey to a mixture of remanence carriers with a wide range of grain-sizes. Thermal demagnetization curves of the soft ( $< 0.1$  T), medium (0.1–0.3 T) and hard (0.3–1.2 T) coercivity fractions of sample P01b show similar

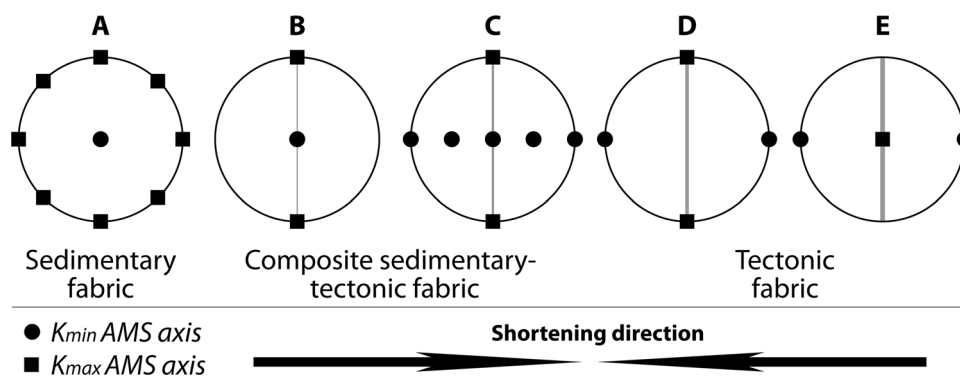


**Fig. 6** Schematic illustration of the evolution of the AMS ellipsoid (equal-area lower hemisphere projections) in response to layer parallel shortening (after Saint-Bezar et al. 2002; Weil and Yonkee 2009). Stage A: Purely sedimentary fabric; stages B and C:

Composite sedimentary-tectonic fabric; stages D and E: Tectonic fabric. Black arrows indicate shortening direction related to the lower hemisphere plots

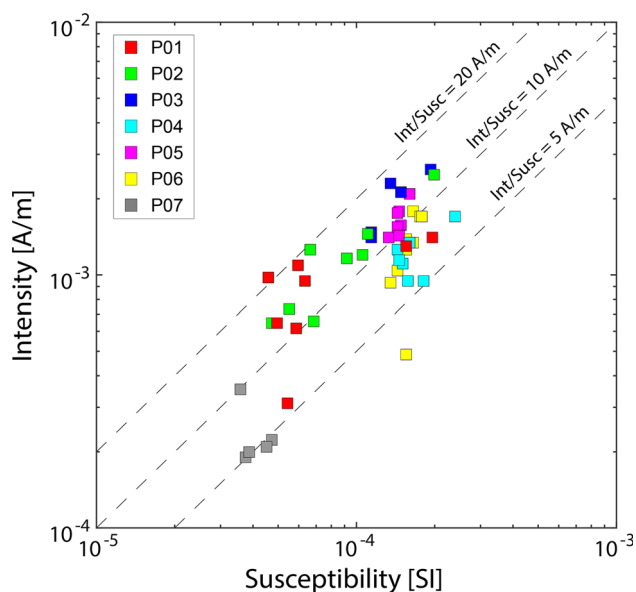


**Fig. 7** Bulk susceptibility versus magnetic intensity plot for all sampling sites. Color code is given in the legend. Dashed lines denote intensity normalized for susceptibility, which serves as a first-order indicator for variations of magnetic carrier

proportion of the different coercivity fractions with distinct unblocking curves (Fig. 8a) Soft fraction shows a minor change in slope at 350 °C, suggesting certain contents of low-coercivity maghemite or titanomagnetite. The main decay of the soft component occurs at 500–560 °C, with almost no magnetization left in the interval 560–650 °C, indicating low-coercivity magnetite (i.e., MD magnetite). The medium and hard fractions of the IRM decrease monotonically up to 620 °C and demagnetize completely at 650 °C, pointing to hematite with some Ti content.

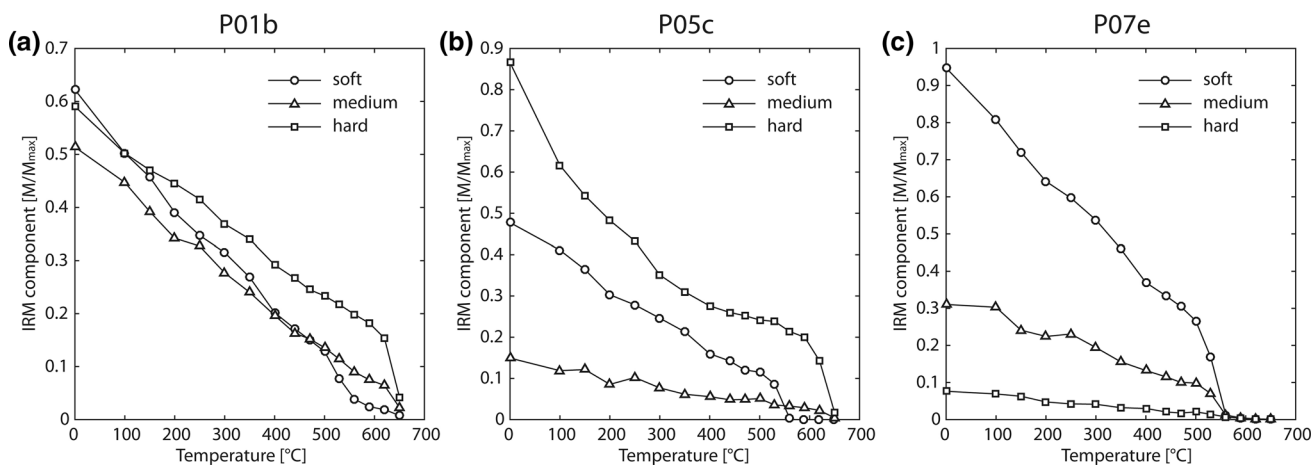


**Fig. 8** Cross-component IRM thermal demagnetization curves for three selected samples. Soft, medium and hard coercivity fractions relate to 0.1, 0.3 and 1.2 T, respectively. **a, b** Samples P01b and P05c (Pestehleigh Formation: continental red beds) show a mixture of low-

Individual demagnetization curves of cross-component IRM of sample P05c indicate similar ferromagnetic carriers although in different proportions (Fig. 8b): Magnetization is mainly carried by hard coercivity minerals, followed by low coercivity minerals and negligible intermediate coercivity fraction. Minor changes in demagnetization curve slope of the soft fraction at 150 °C and 350 °C point toward titanomagnetite and low-coercivity maghemite as potential carriers. Abrupt and complete demagnetization at 530–560 °C indicates magnetite. The medium fraction is initially rough but generally decreases linearly towards 640 °C indicating hematite with coercivities between 0.1 and 0.3 T. The hard fraction decreases steeply until 150 °C, pointing towards goethite. The high temperature fraction demagnetizing completely at 650 °C indicates hematite.

Demagnetization curves of sample P07e demonstrate that magnetite is the main carrier in the carbonates of this site (Fig. 8c): All individual curves almost entirely demagnetize at 560 °C with the soft fraction being the most intense, potentially indicating the dominance of multi domain magnetite. Hematite only contributes ~ 1% of the total IRM. Minor changes in demagnetization curve slopes of the soft and medium fractions point toward titanomagnetite and low-coercivity pyrrhotite or maghemite.

Only sample P05c showed a distinctive decrease of intensity of the hard fraction at very low temperatures (80–120 °C) suggesting the presence of goethite (Fig. 8b). However, goethite often only contributes to IRM as a result to an induced field larger than 1.5 T (Lowrie and Heller 1982). This means that occurrences of goethite in tested samples might not be represented by the cross-component IRM demagnetization curves. Nevertheless, goethite may still be detectable in the NRM demagnetization curves due to its very low Curie and Néel temperatures.

coercivity magnetite and hematite with a large range of coercivities. **c** Sample P07e (Chehel Kaman: white carbonates) indicates low- to medium-coercivity magnetite as magnetic carrier

In general, a clear occurrence of magnetite and hematite is detected, whereas the presence of pyrrhotite, maghemite and goethite is speculative due to a lack of indicative Curie temperatures for these phases.

#### 4.1 Paleomagnetic directions

Figure 9 illustrates three typical demagnetization curves of the NRM for samples P02b, P03 g and P05d including Zijderveld plots and normalized intensity. Most demagnetized samples reveal a low-temperature or low-AF component, respectively. Pure thermal demagnetization leads to loss of  $\sim 50\%$  of the NRM at around  $200\text{ }^{\circ}\text{C}$  (Fig. 9a).

Further demagnetization reveals a single static component of magnetization that gets completely demagnetized at  $620\text{ }^{\circ}\text{C}$ . AF demagnetization of the NRM results in a severe loss of 40–60% of the magnetization at alternating fields of  $< 20\text{ mT}$  (Fig. 9b, c). Sample P02b reveals further demagnetization above  $100\text{ mT}$  with a remaining magnetic intensity of 10% at an alternating field of  $200\text{ mT}$  (Fig. 9b). Further thermal demagnetization of the same sample up to  $550\text{ }^{\circ}\text{C}$  unblocks a high-coercivity component with a reverse orientation above  $400\text{ }^{\circ}\text{C}$  heating. The demagnetization curve of sample P05d shows that  $\sim 50\%$  of the magnetization is related to a high-coercivity component that could not be removed by AF demagnetization

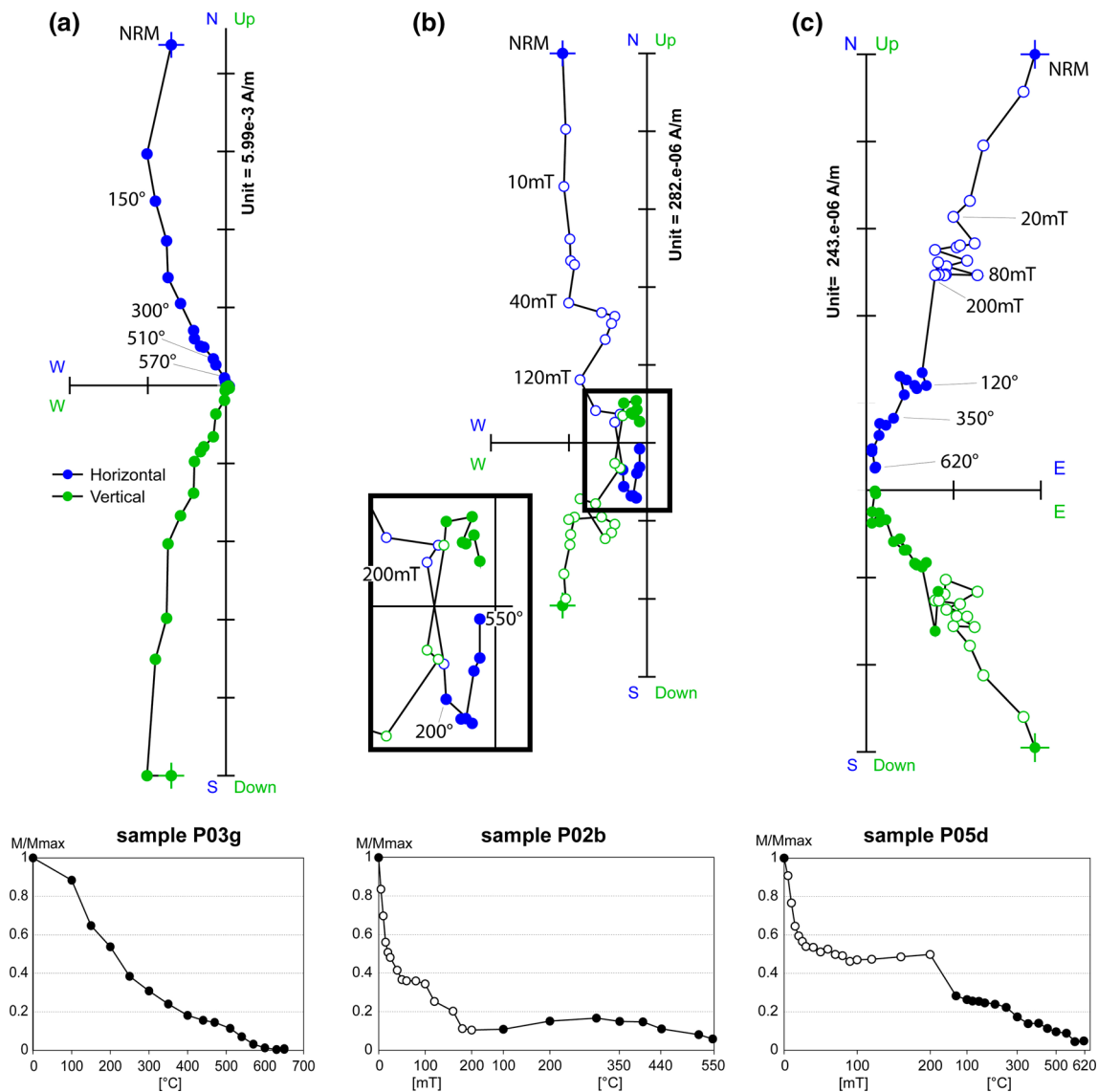


**Fig. 9** Representative demagnetization curves (tilt corrected) and related intensity plots. Blue and green points represent the vertical and horizontal projections of the magnetic direction (after Zijderveld 1967). Full circles indicate thermally demagnetized steps, empty circles denote AF demagnetization. **a** Pure thermal demagnetization

curve of sample P03 g resulting in normal ChRM. **b** Mixed AF and thermal demagnetization curve of sample P02b showing reverse ChRM. **c** Mixed demagnetization showing normal ChRM of sample P05d

(Fig. 9c). Magnetic intensity drops to 25% of its initial value by further heating to 80 °C, indicating the presence of goethite or viscous magnetization. A single static normal magnetic component is then revealed by stepwise heating up to 620 °C (Fig. 9c). In all samples, characteristic remanent magnetization (ChRM) has been defined as the highest-temperature component observed.

A distinct low-temperature or low-AF component has been detected in 43 samples (Fig. 10). Correcting the component directions for bedding tilt results in clustering around a mean declination of 3.6° and a mean inclination of 43.5° with a Fisher precision parameter of  $k = 13.64$  and a radius of circle of confidence of  $\alpha_{95} = 6.1^\circ$ . Uncorrected directions cluster with statistical parameters of  $k = 22.31$  and  $\alpha_{95} = 4.7^\circ$  and average along an orientation with a declination of 356.7° and an inclination of 53.7° (Fig. 10). These data suggest that the low-temperature, low-AF components developed after tectonic folding of the Kalat syncline and are a result of the recent Earth's magnetic

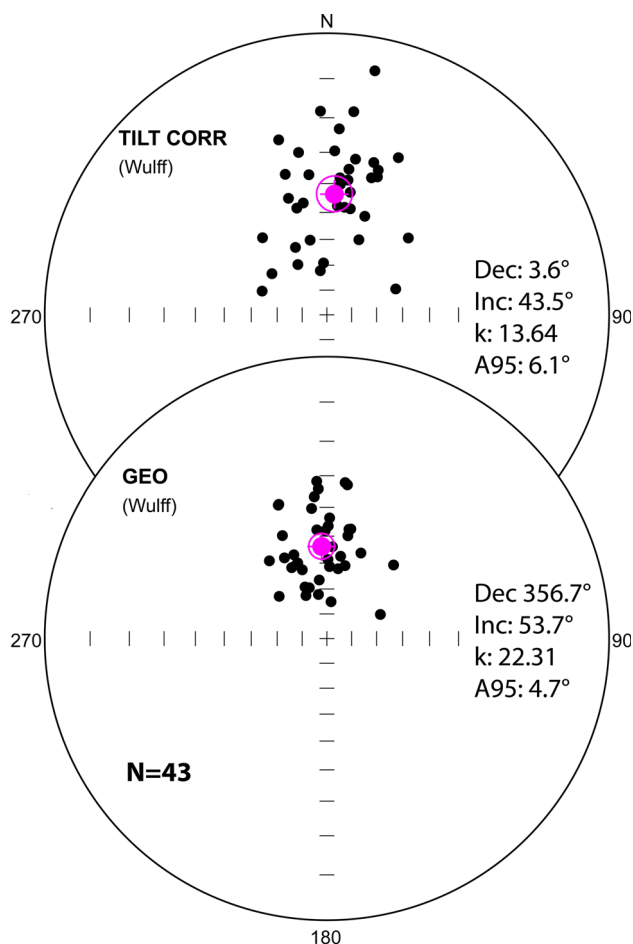


**Fig. 10** Equal-area lower hemisphere projection of the low-temperature/AF component of 43 samples. Top: Magnetic directions corrected for bedding tilt. Bottom: No tectonic correction. Pink circle indicates mean direction. *Dec* declination, *Inc* inclination, *k* precision parameter,  $\alpha_{95}$  confidence angle

field that exhibits an inclination of 53° for a latitude of 37°N and a longitude of 60°E (<http://www.ngdc.noaa.gov/geomag-web/#igrfwmm>).

A well-characterized ChRM component has been found in ~ 50% (48/93) of demagnetized samples (Table 1). From the ChRM directions, the mean paleomagnetic direction for every site has been obtained by using Fisher (1953) statistics (Fig. 11a–g). The ChRM mean direction for every site has been calculated with reversed directions transposed to normal. Exact location, lithology, mean orientation and according statistical parameters of every site are listed in Table 1. Sites P06 and P07 only exhibit two ChRM directions and were therefore excluded from further consideration (Fig. 11f and g). Declination and inclination of mean directions of transposed ChRM of sample sites P01–P05 range between 2.4–27.9° and 26.1–47.3°, respectively (Fig. 11a–e). The overall mean of all relevant site-mean directions (P01–P05) is oriented along a declination of 12.5° with an inclination of 37.3°, where  $k = 10.2$  and  $\alpha_{95} = 7.1^\circ$  (Fig. 12a). All measured directions are separated into normal and reverse oriented partitions to test the primary origin of the ChRM (Fig. 12b, c). Tilt-corrected normal directions show a mean orientation with a declination of 4.8° and an inclination of 38° (Fig. 12b). The tilt-corrected reverse ChRM mean in transposed form has a declination of 33.5° and an inclination of 37.5° (Fig. 12c). Accordingly, a reversal test including sites P01–P05 was performed resulting in an angle of  $\gamma = 22^\circ$  between the mean directions of the normal and reverse polarities (McFadden and McElhinny, 1990). The obtained angle  $\gamma$  is larger than the critical angle  $\gamma_c = 20^\circ$  indicating a negative reversal test for the two separate clusters of orientations. This identifies potential magnetic component overlap (overprint) of samples collected from the clastic Pestheleigh Formation.

## 4.2 Magnetic fabric

Before demagnetization, AMS ellipsoids have been obtained for samples from every site (Fig. 13; Table S1 in supplementary materials). The resulting AMS ellipsoids then can be compared to conceptual models for the evolution of AMS fabric as a result of horizontal shortening to infer local strain/stress patterns (Fig. 6). Measured AMS ellipsoids of sample sites P01–P07 show a range of different patterns from sedimentary to tectonically overprinted fabrics. P02 and P05 show maximum AMS axis scattered in the horizontal plane, although statistically clustering along 90° and 300°, respectively, with a roughly vertical minimum AMS axis (Fig. 13b, e). These AMS patterns describe the initial transition from purely sedimentary to composite sedimentary-tectonic fabric (stage A to stage B; Fig. 6). Sites P01, P03 and P04 are

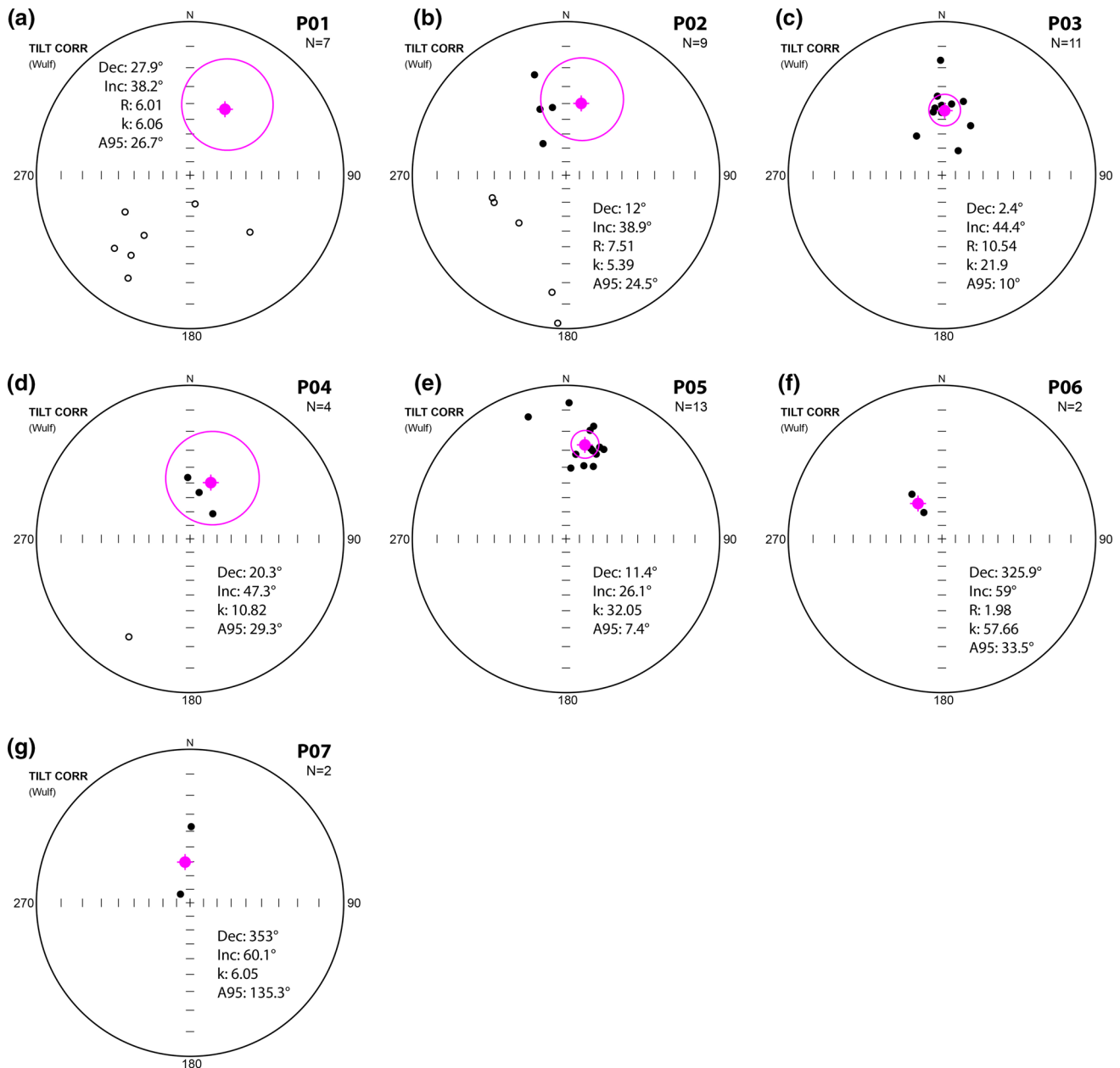


**Fig. 11 a–g** ChRM directions of each site (P01–P07) projected onto an equal-area lower hemisphere. Pink circles: Mean direction and confidence circle of transposed magnetic directions. Pink circles:

Overall mean and confidence circle of all site-mean directions. *Dec* declination, *Inc* inclination, *k* precision parameter,  $\alpha_{95}$  confidence angle

characterized by clear alignment of the maximum AMS axis in the horizontal plane with a vertical minimum axis, scattering slightly along a vertical plane normal to the maximum axis (Fig. 13a, c, d). These patterns represent composite sedimentary-tectonic fabric (stage B and C; Fig. 6). Finally, sites P06 and P07 illustrate alignment of maximum and minimum AMS ellipsoid axis both in the horizontal plane (Fig. 13f, g), where site P07 shows composite sedimentary-tectonic fabric between stage C and D (Fig. 6) and P06 indicating tectonic fabric overprint (stage D to E; Fig. 6).

The corrected degree of anisotropy  $P$  (parameters are defined in Table S1) is higher for carbonate samples of site P07, indicating that those high values are controlled by rock composition (Fig. 13h). Other than P07,  $P$  does not show any distinctive correlation for different sites, suggesting that it is mainly strain controlled or dependent on the bulk susceptibility (see Table S1 in supplementary materials). Calculated values of the shape parameter  $T$  (Jelinek 1981) scatter from  $-1$  (prolate) to  $1$  (oblate) with only site P06 showing purely oblate (tectonic) shapes of AMS ellipsoids (Fig. 13i). Conducted  $f$  and elongation

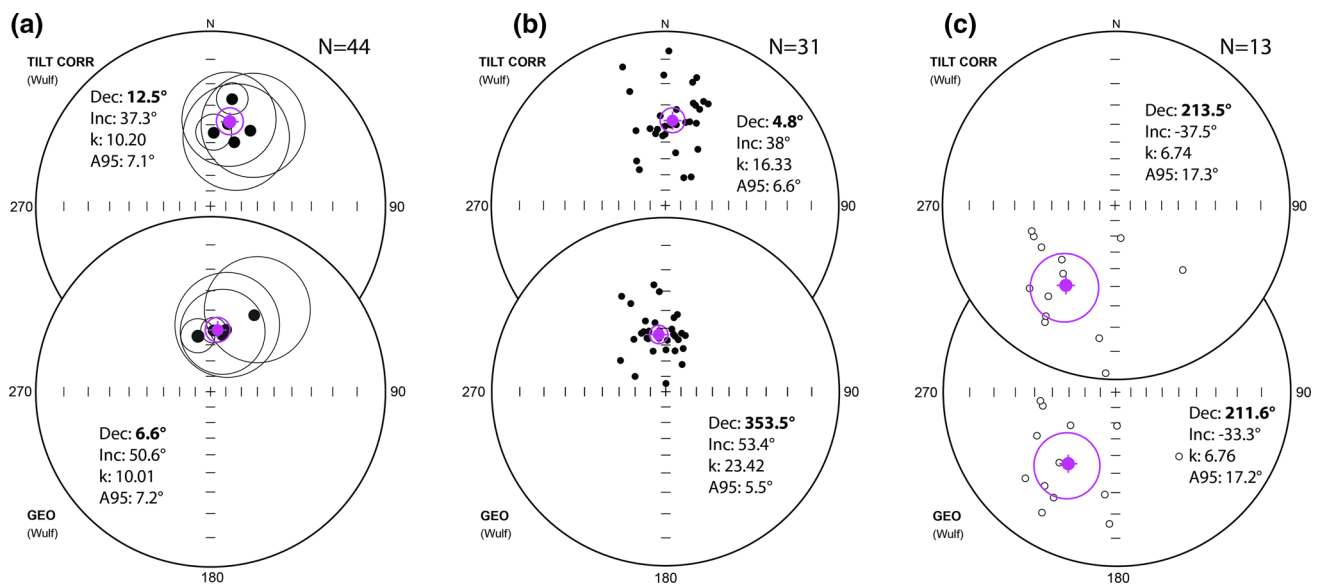


**Fig. 12** Overall statistics of site measurements in geographic and tilt-corrected coordinates (Fig. 11a). **a** Transposed mean directions of sample sites P01–P05. **b** Normal oriented measurements of sites P02–P05. **c** Reverse oriented measurements of sites P01 m, P02 and P04.

tests on all specimens demonstrate that results are statistically significant, except for specimens of site P07, which show very low  $f$  values ( $< 3.48$ ) and a large  $e_{31}$  angle ( $> 26.5^\circ$ ; see Table S1).

## 5 Numerical model

Additional to the magnetic measurements, we conducted a simple numerical experiment of three-dimensional multi-layer folding in order to understand the potential effect of folding dynamics on local vertical-axis rotation. It is assumed that the clastic, silt-dominated Pestehleigh Formation represents a relatively weak stratal layer in between mechanically stronger carbonate lithologies, that are the Cretaceous Kalat Formation below and the Paleogene Chehel Kaman Formation above. Viscous flow and vertical-axis rotation within the mechanically weak layer are tracked during folding of the multi-layer experiment. The obtained results can then be compared to the paleomagnetic measurements to discuss whether the observed paleomagnetic rotations and AMS data fit the deformation and stress field predicted by the numerical experiment.

### 5.1 Mathematical description and model setup

The experiment is carried out with a three-dimensional numerical code based on the finite different method with a fully-staggered Eulerian grid and freely advecting Lagrangian markers carrying rock information (I3ELVIS;

Pink circles: Overall mean and confidence circle of all site-mean directions. *Dec* declination, *Inc* inclination, *k* precision parameter,  $\alpha_{95}$  confidence angle

Gerya 2010; Gerya and Yuen 2007). The numerical model solves the equations for conservation of mass and momentum (Stokes equation) with an efficient OpenMP-parallelized multigrid solver applying a simple linear viscous rheology.

The experiment has been set up to reproduce an elongated, doubly-plunging open syncline in size and shape comparable to the Kalat syncline (Figs. 2, 3, 4 and 5). The Eulerian model box measures 30·14.8·58.8 km in  $x$ -,  $y$ - and  $z$ -direction (Fig. 14a) with a nodal resolution of 101·149·197, respectively, and 8 Lagrangian markers per nodal cell. To investigate the potential viscous flow in the Paleocene Pestehleigh Formation, a multilayer geometrical setup has been introduced that represents the uppermost crustal sequence outcropping along the Kalat syncline (Fig. 2). Initial layering of the experiment includes two strong horizons with a viscosity of  $10^{23}$  Pa·s separated and embedded within a weak matrix with a viscosity of  $10^{20}$  Pa·s (Fig. 14a). Both strong layers have an initial vertical thickness of 2 km and are introduced at  $y = 7.3$ – $9.3$  km and  $y = 10.3$ – $12.3$  km. The strong layers represent the rigid Cretaceous carbonate formation below (Kalat Formation) and the Paleogene white carbonates above (Chehel Kaman Formation) the mechanically weaker red clays and siltstones of the Paleocene Pestehleigh Formation.

To obtain a doubly-plunging syncline, layers have been shortened horizontally in two perpendicular directions. Velocity boundary conditions prescribe material influx along all lateral boundaries resulting in a total shortening rate of 1 cm/year along the  $x$ -axis and a total shortening

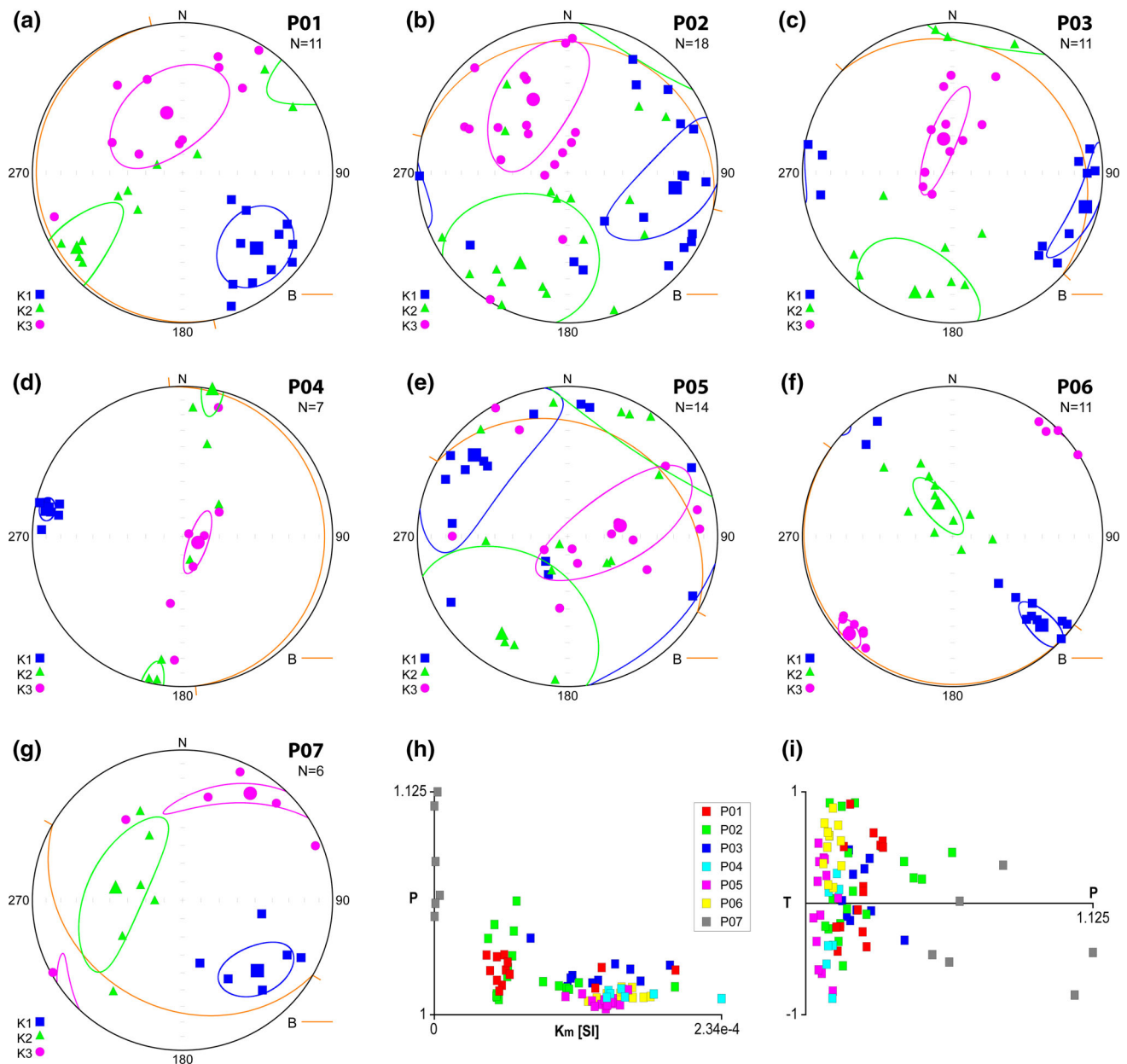


**Fig. 13 a–g** Equal-area lower hemisphere projection of the AMS ellipsoids for each sample site (P01–P07). Blue squares: maximum susceptibility axis (K1); Green triangles: intermediate susceptibility axis (K2); Pink circles: minimum susceptibility axis (K3). Red lines: Bedding planes. Specimens of all sites are statistically significant except for P07 (see Table S1). **h** Mean susceptibility versus degree of

corrected anisotropy ( $P$ ) plot. All sample sites show similar degree of anisotropy except carbonate samples of site P07. **i** Plot of degree of corrected anisotropy ( $P$ ) versus shape factor ( $T$ ). All sites show both oblate and prolate shapes of magnetic fabric except site P06 (only oblate) indicating full tectonic overprint

rate of 0.5 cm/year along the  $z$ -axis (Fig. 14a). The top velocity boundary prescribes material outflow by a vertical velocity of  $-0.62$  cm/yr to assure conservation of volume (mass) within the Eulerian model box. The bottom boundary prescribes zero perpendicular material flux. All boundaries exhibit free-slip velocity conditions in both boundary-parallel directions, which means zero shear stresses across the boundaries. The numerical experiment run with timesteps of 5 kyr.

## 5.2 Modelling results

Two-axial horizontal shortening of the multilayer stack described above for a time span of 1.35 Myr resulted in parallel folding of the strong layers and viscous flow due to bedding-parallel shearing of the weak layer in between. Removal of the uppermost weak layer allows recognizing the fold geometry, defining an open doubly-plunging syncline (Fig. 14a). Fold wavelengths in  $x$ - and  $z$ -directions

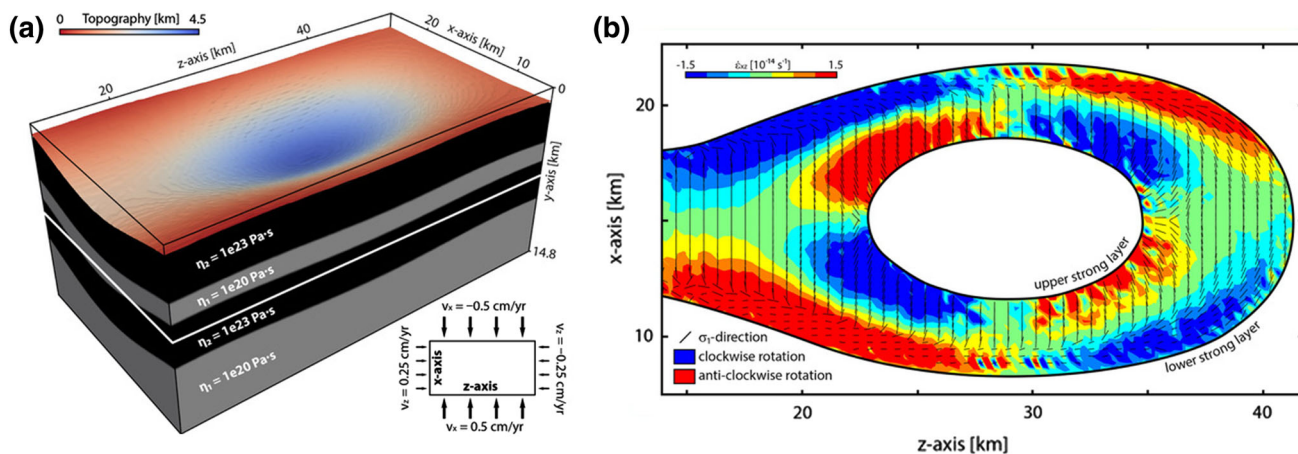


**Fig. 14** Numerical model of viscous multi-layer folding. **a** 3D illustration after 1.35 Myr of shortening. Grey: Weak layers with a viscosity of  $\eta_1 = 10^{20}$  Pa·s. Black: Strong layers with a viscosity of  $\eta_2 = 10^{23}$  Pa·s. Topography of the top of the upper strong layer presents a doubly-plunging syncline. Bottom right: Map view of model box with applied velocity boundary conditions. White line indicates location of horizontal slice shown in **b**. **b** Colored area

are comparable to strike-orthogonal (NNE–SSW) and along-strike (WNW–ESE) folding wavelengths of the Kalat syncline, respectively (Fig. 2, 3, 4 and 5). Figure 14b illustrates the horizontal shear strain rate (total vertical-axis rotation) and principal stress directions within the interbedded weak horizon in a plane cutting the model box horizontally at  $y = 7.4$  km (Fig. 14a). Vertical-axis shear strain rate is defined as

$$\dot{\epsilon}_{xz} = \dot{\epsilon}_{zx} = \frac{1}{2} \left( \frac{\partial v_x}{\partial z} + \frac{\partial v_z}{\partial x} \right), \quad (1)$$

where  $v_x$  and  $v_z$  are velocities in  $x$ - and  $z$ -direction and  $x$  and  $z$  denote spatial coordinates.

Vertical-axis rotational shear strain rates within the weak horizon representing the Pestehleigh Formation show two distinctive patterns depending on their stratigraphic position. At the top of the weak layer, close to the contact with the upper strong layer, viscous flow shows clockwise rotational shear strain rates in the lower left and the upper right quarter and counter-clockwise rotation in the upper left and lower right quarter (Fig. 14b). A contrary scheme of vertical-axis rotation occurs at the base of the weak horizon, along the contact to the underlying strong layer. There, viscous flow undergoes clockwise rotation in the upper left and lower right quarters and counter-clockwise rotation in the lower left and upper right parts, respectively (Fig. 14b).

Principle stress within the horizontal plane cross-cutting at  $y = 7.4$  km show an orientation parallel to the  $x$ -axis (main shortening direction) where shear strain rates are close to zero, which is close to the stratigraphic center

indicates shear strain rate within intermediate weak layer. Blue indicates clockwise vertical-axis rotation. Red denotes counter-clockwise vertical-axis rotation. Black lines show the orientation of the maximum principal stress axis. The shear strain rate and stress pattern strongly depend on the stratigraphic position of the weak intermediate horizon

(Fig. 14b). Towards the strong layers, principle stress axes get deflected depending on the viscous vertical-axis rotation within the weak horizon. A typical pattern of stress orientation can be detected in the right part of the horizontal slice (Fig. 14b): (i) Along the contact with the upper strong layer, maximum principle stress axes tend to deflect inwards directing towards the syncline center. (ii) Close to the contact with the lower strong layer, maximum principle stresses rotate towards parallel to the contact, away from the syncline center.

## 6 Discussion

In the following section, we first discuss the applicability of the presented paleomagnetic data. Then, measured paleomagnetic directions are discussed with regard to potential vertical-axis rotation in the East Kopet Dagh mountains (e.g., Hollingsworth et al. 2010; Mattei et al. 2019) and the Alborz (e.g., Cifelli et al. 2015; Mattei et al. 2017). Finally, we compare paleomagnetic results with the obtained 3D numerical experiment to evaluate the effects of folding-related flow on local vertical-axis rotation and principle stress directions.

### 6.1 Quality of the paleomagnetic data

Cross-component IRM measurements showed that medium- to high-coercivity hematite is the main carrier of magnetic components in the continental Pestehleigh Formation (Fig. 8a, b). Hematite has high Néel temperature

and saturates at high magnetic fields ( $\approx 675$  °C, 1.5–5 T; Lowrie 1990 and references therein) and therefore serves as good potential carrier of stable ChRM components. Continental red bed sandstones can be prone to hematite-related remagnetization due to dissolution of iron-bearing silicates (Hodych et al. 1985; Jiang et al. 2017). Therefore, we focused on sampling fine-grained clay and siltstones to avoid chemical magnetic overprint. The presence of goethite is not demonstrated clearly by cross-component IRM demagnetization curves but can be inferred from combined temperature-AF demagnetization curves of the NRM (Fig. 9b, c). However, the effect of (potentially secondary) goethite on the ChRM component is removed efficiently due to its low Curie and Néel temperatures of  $\sim 120$  °C (Ozdemir and Dunlop 1996). In general, magnetic mineralogy of sample sites P01–P06 (Pestehleigh Formation) is similar to lithologies sampled to reveal vertical-axis rotation in the Alborz (Mattei et al. 2017).

Cross-component IRM demagnetization of carbonate samples from site P07 mainly indicate magnetite with low coercivities as magnetic carrier (Fig. 8c). Furthermore, samples of site P07 exhibit relatively low NRM intensities and bulk susceptibilities in contrast to the continental sediments of site P01–P06 (Fig. 7). Independent of the quality of the magnetic data, site P06 and P07 only comprise two samples each that reveal a paleomagnetic direction due to a stable ChRM component (Fig. 11f, g). Thus, these two sites have not been considered when calculating the overall paleomagnetic directions (Fig. 12) and their resulting site-specific paleomagnetic rotation is ignored during further discussion. For sites P01–P05, two-thirds of all measured samples revealed a stable ChRM component (Table 1). A fold test was not possible to conduct given the very shallow dips of bedding within the Pestehleigh Formation around the Kalat syncline. Nevertheless, the occurrence of normal and reverse polarities at site level in sites P01, P02 and P04 reinforces the pre-tectonic character of the collected data (Fig. 12b, c). The applied reversal test (McFadden and McElhinny 1990) is negative (see Sect. 4.1), indicating at least partial magnetic overprint (Fig. 12b, c). Therefore, ChRM orientations are discussed in the following with respect to potential magnetic overprint or at least partial incomplete isolation of the ChRM directions.

Ellipsoids of the anisotropy of the magnetic susceptibility (AMS) show good clustering for each sample site except for sites P02 and P05, where the clusters of the different ellipsoid axes are more dispersed (Fig. 13). All sites show a certain amount of tectonic overprint of the magnetic fabric with the minimum AMS ellipsoid axis parallel to the strike of the mountain belt and the maximum AMS ellipsoid axis oriented into the direction of horizontal shortening (e.g., Weil and Yonkee 2009).

## 6.2 Vertical-axis rotation of the East Kopet Dagh

The Kopet Dagh mountain belt resulted from Oligocene–Miocene tectonic inversion of a mainly Jurassic intracontinental rift situated on the Turan plate, along the southern margin of the Eurasia continent (Golonka 2004; Lyberis and Manby 1999). In this study, we gathered paleomagnetic directions in the East Kopet Dagh to test whether shortening and uplift in this part of the orogen was accompanied by vertical-axis rotation, as inferred from its arcuate shape (Fig. 1) and as proposed by earlier studies (e.g., Hollingsworth et al. 2010). To calculate vertical-axis rotation, paleomagnetic directions presented here have to be compared to Paleocene paleomagnetic directions from stable southern Eurasia. Cretaceous to Paleocene rocks in the (today) Turkmen part of the northwestern Kopet Dagh revealed a paleomagnetic direction with a declination of  $12.2^\circ$  and an inclination of  $49.7^\circ$  (Bazhenov 1987). This direction agrees with the paleomagnetic direction calculated from the mean paleomagnetic pole for stable Europe with a declination of  $12.5^\circ$  and an inclination of  $50.1^\circ$  for the Paleogene (Gordon and Van der Voo 1995). The overall mean paleomagnetic direction (normal and reverse orientations) obtained from Paleocene red beds of the Kalat syncline in the East Kopet Dagh shows a declination of  $12.5^\circ$  with an inclination of  $37.3^\circ$  (Fig. 12a). Hence, this data would suggest that the Kalat synclinal structure has not been prone to vertical-axis rotation other than the rotation related to the stable Eurasian continental plate since Paleocene times. The relatively flat inclination in contrast to the expected stable Eurasia paleomagnetic inclination might be due to inclination shallowing typically observed in continental red bed formations (Garces et al. 1996; Tan and Kodama 2002). However, an applied reversal test indicating that ChRM components are partially overprinted, which makes this interpretation unreliable, as magnetic directions may be overprinted after tectonic rotation. Taking into consideration only the reverse ChRM directions, presumably not overprinted, the resulting transposed mean direction exhibits a declination of  $33.5^\circ$  with an inclination of  $37.5^\circ$  (Fig. 12c). With respect to paleopoles for stable Europe with a declination of  $12.5^\circ$ , this would indicate a clockwise vertical-axis rotation of  $21^\circ$ . However, the reversed directions show a wide clustering and a  $\alpha_{95}$ -angle of  $17.3^\circ$ .

We interpret that at least the reversed directions have been acquired shortly after Paleocene sediment accumulation and have remained stable since then, whereas parts of the normal directions have been overprinted due to tectonic activity, resulting in a negative reversal test. This would imply that the reverse orientations can be used to calculate vertical-axis rotations since the Paleocene

(depositional age of the Pestehleigh Formation) and that the normal orientations are the result of magnetic overprint having taken place after the main phase of regional deformation. However, variations in mean transposed normal directions may indicate late stage (after magnetic overprint) tectonic activity.

Paleomagnetic data from the Alborz mountains suggest syn-orogenic oroclinal bending of the range as a result of the indentation of the rigid South Caspian Basin (Mattei et al. 2017). In the East Alborz (at longitudes of  $\sim 58^\circ\text{E}$ ), south of the Kopet Dagh, (Mattei et al. 2017) measured paleomagnetic declinations of  $22.5^\circ$  in the Miocene Upper Red Formation, resulting in a clockwise rotation of  $18.4 \pm 7.9^\circ$  since the Miocene. Data from the Kopet Dagh indicates a clockwise rotation of  $19.4^\circ$  and  $14.3^\circ$  since the Cretaceous and Paleocene, respectively (Mattei et al. 2019). Their data match well vertical-axis rotation values for only reverse direction (Fig. 12c) since the Paleocene calculated here ( $21^\circ$ ). Furthermore, Mattei et al. (2017) calculated a counter-clockwise rotation of  $21.1 \pm 11.6^\circ$  at longitudes between  $52$  and  $54^\circ\text{E}$  (Fig. 1). These published paleomagnetic rotations suggest that the Kopet Dagh underwent oroclinal bending. Earlier data by Bazhenov (1987) and paleomagnetic results taken as a whole in this study do not reveal any rotation along the northern boundary of the Kopet Dagh mountains. This might indicate that the Kopet Dagh Basin closed in a “scissor tectonic” fashion (Zwaan and Schreurs 2017), where the southern margin rotated clockwise and the northern one remained stable. Thus, clockwise rotations would be expected closer to the tectonic boundary with the East Alborz and especially towards the southeast of the Kopet Dagh. Therefore, further paleomagnetic direction measurements need to be conducted in this area to test whether the Kopet Dagh potentially represents a secondary orocline resulting from superimposed wrenching (Model E from Fig. 17 of Weil and Yonkee 2009).

### 6.3 Local folding kinematics

Although the reverse ChRM mean direction indicates  $21^\circ$  of regional clockwise rotation potentially resulting from oroclinal bending, individual paleomagnetic mean directions of every site (Fig. 11) around the Kalat syncline show a rotational pattern related to the syncline structure (Fig. 15; red arrows). Although partially overprinted or overlapping, this pattern may represent local rotations post-dating major vertical-axis rotation as folding in the Kopet Dagh happened earliest in the Oligocene (Berberian and King 1981; Golonka 2004; Hollingsworth et al. 2010) and maybe even in late Miocene times (Lyberis and Manby 1999). Furthermore, late Miocene growth strata along the northern boundary of the East Kopet Dagh support this

interpretation of a late deformation stage. The site-mean paleomagnetic directions describe a local rotation at each site so that the normal line to the direction points towards the syncline center, i.e. clockwise rotation in the northwest and southeast and anti-clockwise rotation in the northeast and southwest parts of the syncline (Fig. 15). Directions of shortening inferred from the AMS ellipsoid orientation at every site (Fig. 13) show a similar picture (Fig. 15; blue arrows). The overall direction of shortening calculated as an average of all site AMS ellipsoid measurements is oriented towards  $32^\circ$ , which is perpendicular to the overall strike of the Kopet Dagh ( $\sim 120^\circ$ ). Like paleomagnetic directions, AMS ellipsoids are rotated clockwise in the northwest and southeast and anti-clockwise in the northeast and southwest, relatively to the overall mean orientation (Fig. 15).

To test whether this observed pattern of rotation and principle strain/stress orientations can be reproduced and explained by 3D folding dynamics, paleomagnetic data are compared to results of the numerical experiment of multi-layer deformation (Fig. 14). Viscous flow of the relatively weak material in between two stronger layers is characterized by vertical-axis rotational strain rates depending on the vertical and horizontal position (Fig. 14b). Rotational flow close to the lower strong layer reproduces the rotation pattern deduced from paleomagnetic directions (Fig. 15; red arrows). Orientations of numerical principle stress orientations close to the lower strong layer are comparable to the shortening directions calculated from AMS ellipsoids around the Kalat syncline (Fig. 15; blue arrows). AMS data has been demonstrated to reflect the orientation of the strain tensor (Borradaile and Henry 1997). However, it has also been shown that the orientation of the strain tensor is comparable to the one of the stress tensor when investigating claystones and slates (Sagnotti et al. 1994).

The accordance of paleomagnetic results and numerically obtained viscous flow of the weak layer during three-dimensional multi-layer folding in terms of local vertical-axis rotation and principle stress direction helps understanding the structural evolution of the Kalat syncline. Numerical results support the assumption that the Paleocene continental red beds (Pestehleigh Formation) acted as a weak decoupling horizon between the more rigid carbonate-dominant horizons of the Kalat and Chehel Kaman formations and therefore has been able to deform at strain rates large enough to feature measurable local vertical-axis rotations. Rotation strain-rate patterns within the weak interlayer furthermore suggest that sample sites are situated at the stratigraphic base of the Pestehleigh Formation (Fig. 14b). This is true except for site P04, which is stratigraphically located higher up within the Pestehleigh Formation.

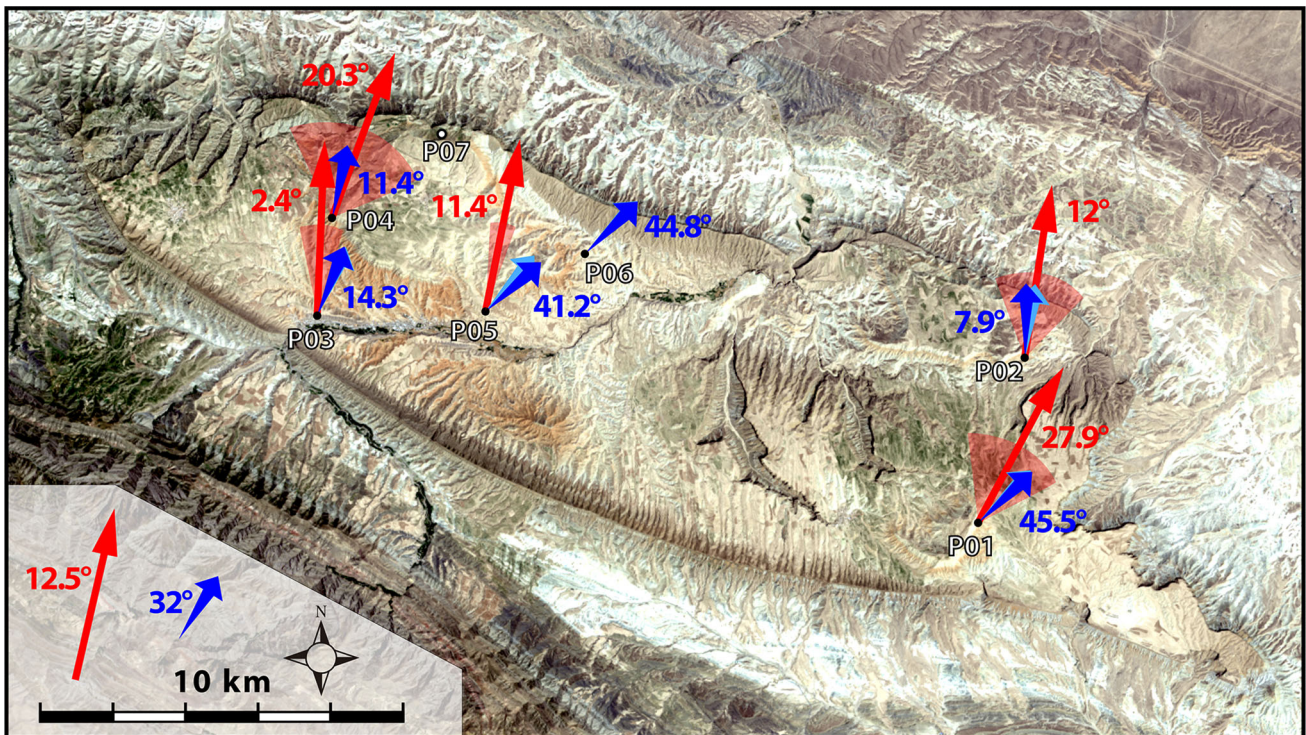


**Fig. 15** Satellite image of the Kalat syncline. Location is outlined by black box in Fig. 2. Red arrows: Paleomagnetic directions including value for declination for sites P01–P05. Red shade: Error of the paleomagnetic direction after Demarest (1983). Blue arrows: Direction perpendicular to the maximum axis of AMS ellipsoids for sites

P01–P06 indicating main shortening (site P07 is statistically not relevant; see Table S1). Light blue arrows: AMS directions corrected for bedding tilt. Bottom left: Legend and overall mean paleomagnetic and AMS directions including values

The pattern of paleomagnetic directions and AMS ellipsoid orientation around the Kalat syncline are a result of three-dimensional folding and related deformation within a relatively weak horizon. The doubly-plunging shape of the syncline might be the result of the complex underlying basement structure. Seismic sections cross-cutting and parallel to the main strike of the Kopet Dagh, i.e. along the shortest and longest syncline axis, respectively, both illustrate the occurrence of basement faults offsetting pre-Jurassic to Jurassic strata (Figs. 3, 4 and 5). Major inherited normal faults strike parallel to the overall Kopet Dagh (Amurskiy 1971) strike and act potentially as reverse thrusts during tectonic inversion (Robert et al. 2014; Ruh and Vergés 2018; Ruh 2019). These faults result from Middle Jurassic rifting along the southern margin of the Turan plate. Another set of rift structures, which strike NNW–SSE, affected the whole Amu Darya Basin during the Triassic (Brunet et al. 2017; Khain et al. 1991). We argue that those two sets of normal faults resulted in stratigraphic thickness variations parallel to and across the Kopet Dagh Basin that enabled the growth of a doubly-plunging syncline during their structural reactivation in the Cenozoic. Forced three-dimensional folding then lead to local vertical-axis rotation within the weak horizon, i.e. the

continental formation, resulting in the particular pattern obtained by paleomagnetic measurements.

## 7 Conclusions

Paleomagnetic directions from continental red beds and white carbonates around the Kalat syncline in the East Kopet Dagh mountains, NE Iran, reveal that ChRM directions may have been overprinted, are not fully isolated or overlap with other components according to a reversals test. The overall mean paleomagnetic direction of all samples exhibits a declination of  $12^\circ$ , indicating no vertical-axis rotation. On the whole, reverse directions suggest a potential clockwise vertical-axis rotation of  $21^\circ$  along the Kalat syncline, comparable to rotation in the South Kopet Dagh. We therefore conclude that reverse directions represent clockwise vertical-axis rotation since the Paleocene and that magnetic directions were partially overprinted after major tectonic rotation. The overall mean direction of shortening inferred from AMS ellipsoids is oriented perpendicular to the present strike of the northern boundary of the Kopet Dagh, that is the Main Kopet Dagh Fault. Individual paleomagnetic and AMS-related shortening

directions show a characteristic pattern with respect to the doubly-plunging syncline shape indicating potential local rotation after magnetic overprint. A numerical model of multi-layer forced folding has been conducted to test the effects of complex folding kinematics on local vertical-axis rotations. The experiment suggests that the clastic red beds (Pestehleigh Formation) acted as a weak interlayer in between more rigid carbonate horizons, which may explain variations of post-overprint vertical-axis rotation for different locations around a growing doubly-plunging syncline.

**Acknowledgements** The authors thank Bjarne Almqvist and an anonymous reviewer for their constructive comments. This work has been supported by Swiss National Science Foundation (Grant Number 2-77297-15). We thank the National Iranian Oil Company who organized field work and the Paleomagnetic Laboratory CCiTUB-ICJTA CSIC where measurements were conducted.

## References

- Afshar, A. (1982). Darreh Gaz geological quadrangle map: 1:250,000. Ministry of Petroleum, National Iranian Oil Company, Exploration and Production, Geological quadrangle map of Iran No. K3. Tehran: Offset Press.
- Afshar, A. (1983). Sarakhs geological quadrangle map: 1:250,000. Ministry of Petroleum, National Iranian Oil Company, Exploration and Production. Tehran: Offset Press.
- Afshar Harb, A., Aghanabati, A., Madjdi, B., Alavi Tehrani, N., Shahrabi, M., Davoudzadeh, M., et al. (1986). Mashhad geological quadrangle map: 1:250,000. Ministry of Mine and Metals, Geological Survey of Iran, Tehran Naqsheh, Tehran.
- Afshar, A., Soheili, M., & Valeh, N. (1984). Kuh-E-Kurkhud geological quadrangle map: 1:250,000. Geological quadrangle map of Iran No. 13. Geological Survey of Iran.
- Allen, M. B., Vincent, S. J., Alsop, G. I., Ismail-zadeh, A., & Flecker, R. (2003). Late Cenozoic deformation in the South Caspian region: effects of a rigid basement block within a collision zone. *Tectonophysics*, 366, 223–239.
- Amurskiy, G. I. (1971). The deep structure of the Kopet Dagh. *Geotectonics*, 1, 34–40.
- Ballato, P., Landgraf, A., Schildgen, T. F., Stockli, D. F., Fox, M., Ghassemi, M. R., et al. (2015). The growth of a mountain belt forced by base-level fall: Tectonics and surface processes during the evolution of the Alborz Mountains, N Iran. *Earth and Planetary Science Letters*, 425, 204–218.
- Bazhenov, M. L. (1987). Paleomagnetism of Cretaceous and Paleogene sedimentary-rocks from the Kopet-Dagh and its tectonic implications. *Tectonophysics*, 136, 223–235.
- Behrouzi, A., Eftekhar-Nezhad, J., Alavi Naini, M., Chaichi, Z., Afsharian Zadeh, A.M., & Ghomashi, A. (1993). Torbat-E -Jam geological quadrangle map: 1:250,000. Geological Survey of Iran, Tehran Naqsheh, Tehran.
- Berberian, M., & King, G. C. P. (1981). Towards a paleogeography and tectonic evolution of Iran. *Canadian Journal of Earth Science*, 18, 210–265.
- Bolourchi, M.H., Mehr Parto, M., Afshar Harb, A., Afaghi, A., Jamshidi, K., Ghandchi, M., et al. (1987). Bojnurd geological quadrangle map: 1:250,000. Ministry of Mine and Metals, Geological quadrangle map of Iran No. J-3, Geological Survey of Iran. Tehran: Offset Press.
- Borradaile, G. J., & Henry, B. (1997). Tectonic applications of magnetic susceptibility and its anisotropy. *Earth-Science Reviews*, 42, 49–93.
- Brunet, M.-F., Ershov, A. V., Korotaev, M. V., Melikhov, V. N., Barrier, E., Mordvintsev, D. O., et al. (2017). Late Palaeozoic and Mesozoic evolution of the Amu Darya Basin (Turkmenistan, Uzbekistan). In M.-F. Brunet, T. McCann, & E. R. Sobel (Eds.), *Geological Evolution of Central Asian Basins and the Western Tien Shan Range*. London: Geological Society.
- Brunet, M. F., Korotaev, M. V., Ershov, A. V., & Nikishin, A. M. (2003). The South Caspian Basin: A review of its evolution from subsidence modelling. *Sedimentary Geology*, 156, 119–148.
- Chadima, M., & Hrouda, F. (2006). Remasoft 30 a user-friendly paleomagnetic data browser and analyzer. *Trav. Geophys.*, XXVII, 20–21.
- Chadima, M., Hrouda, F., & Jelinek, V. (2018). Anisoft: Advanced treatment of magnetic anisotropy data, 5.1.01 ed. AGICO, Inc., Brno, Czech Republic.
- Cifelli, F., Ballato, P., Alimohammadian, H., Sabouri, J., & Mattei, M. (2015). Tectonic magnetic lineation and oroclinal bending of the Alborz range: Implications on the Iran-Southern Caspian geodynamics. *Tectonics*, 34, 116–132.
- Cifelli, F., Caricchi, C., & Mattei, M. (2016). Formation of arc-shaped orogenic belts in the Western and Central Mediterranean: a palaeomagnetic review. *Palaeomagnetism in Fold and Thrust Belts: New Perspectives*, 425, 37–63.
- Demarest, H. H. (1983). Error analysis for the determination of tectonic rotation from paleomagnetic data. *Journal of Geophysical Research*, 88, 4321–4328.
- Eftekhar-Nezhad, J., Aghanabati, A., Nazer, N.H., Hamedi, A., Vaezipour, M.J., Nabavi, et al. (1992). Jajarm geological quadrangle map: 1:250,000. Geological Survey of Iran, Tehran Naqsheh, Tehran.
- Fisher, R. (1953). Dispersion on a sphere. *Proceedings of the Royal Society of London, Series-A*, 217, 295–305.
- Garces, M., Pares, J. M., & Cabrera, L. (1996). Further evidence for inclination shallowing in red beds. *Geophysical Research Letters*, 23, 2065–2068.
- Gerya, T. (2010). *Introduction to Numerical Geodynamic Modelling*. Cambridge: Cambridge University Press.
- Gerya, T. V., & Yuen, D. A. (2007). Robust characteristics method for modelling multiphase visco-elasto-plastic thermo-mechanical problems. *Physics of the Earth and Planetary Interiors*, 163, 83–105.
- Golonka, J. (2004). Plate tectonic evolution of the southern margin of Eurasia in the Mesozoic and Cenozoic. *Tectonophysics*, 381, 235–273.
- Gordon, R. G., & Van der Voo, R. (1995). Mean paleomagnetic poles for the major continents and the Pacific plate. In T. J. Ahrens (Ed.), *Global Earth Physics: A Handbook of Physical Constants* (pp. 225–239). Washington, D.C: AGU.
- Hodych, J. P., Patzold, R. R., & Buchan, K. L. (1985). Chemical remanent magnetization due to deep-burial diagenesis in oolitic hematite-bearing ironstones of Alabama. *Physics of the Earth and Planetary Interiors*, 37, 261–284.
- Hollingsworth, J., Fattahi, M., Walker, R., Talebian, M., Bahroudi, A., Bolourchi, M. J., et al. (2010). Oroclinal bending, distributed thrust and strike-slip faulting, and the accommodation of Arabia-Eurasia convergence in NE Iran since the Oligocene. *Geophysics Journal International*, 181, 1214–1246.
- Hollingsworth, J., Jackson, J., Walker, R., Gheitanchi, M. R., & Bolourchi, M. J. (2006). Strike-slip faulting, rotation, and along-strike elongation in the Kopeh Dagh mountains, NE Iran. *Geophysics Journal International*, 166, 1161–1177.

- Hollingsworth, J., Jackson, J., Walker, R., & Nazari, H. (2008). Extrusion tectonics and subduction in the Eastern South Caspian region since 10 Ma. *Geology*, *36*, 763–766.
- Hrouda, F. (1982). Magnetic anisotropy of rocks and its application in geology and geophysics. *Geophysical Survey*, *5*, 37–82.
- Jalilian, M., Etemadi, N., Afsharian Zadeh, A., Manoucherhi, M., Vaezipour, M.J., Alavi Tehrani, N., et al. (1992). Torbat-E-Heydarieh geological quadrangle map: 1:250,000. Geological quadrangle map of Iran No. K-5. Geological Survey of Iran, Tehran Naqshah, Tehran.
- Jelinek, V. (1981). Characterization of the magnetic fabric of rocks. *Tectonophysics*, *79*, 163–167.
- Jiang, Z. X., Liu, Q. S., Dekkers, M. J., Zhao, X., Roberts, A. P., Yang, Z. Y., et al. (2017). Remagnetization mechanisms in Triassic red beds from South China. *Earth and Planetary Science Letters*, *479*, 219–230.
- Kavoosi, M. A., Lasemi, Y., Sherkati, S., & Moussavi-Harami, R. (2009). Facies analysis and depositional sequences of the upper Jurassic Mozduran Formation, a carbonate reservoir in the Kopet Dagh Basin, NE Iran. *Journal of Petroleum Geology*, *32*, 235–259.
- Khain, V. E., Sokolov, B. A., Kleshchev, K. A., & Shein, V. S. (1991). Tectonic and geodynamic setting of oil and gas basins of the Soviet-Union. *AAPG Bulletin*, *75*, 313–325.
- Kirschvink, J. L. (1980). The least-squares line and plane and the analysis of paleomagnetic data. *Geophysical Journal of the Royal Astronomical Society*, *5*, 62, 699–718.
- Lowrie, W. (1990). Identification of ferromagnetic minerals in a rock by coercivity and unblocking temperature properties. *Geophysical Research Letters*, *17*, 159–162.
- Lowrie, W., & Heller, F. (1982). Magnetic properties of marine limestones. *Review of Geophysics*, *20*, 171–192.
- Lowrie, W., & Hirt, A. M. (1986). Paleomagnetism in arcuate mountain belts. In F. C. Wezel (Ed.), *The origin of arcs* (pp. 141–158). Amsterdam: Elsevier.
- Lyberis, N., & Manby, G. (1999). Oblique to orthogonal convergence across the Turan block in the post-Miocene. *AAPG Bulletin*, *83*, 1135–1160.
- Maggi, A., Jackson, J. A., McKenzie, D., & Priestley, K. (2000). Earthquake focal depths, effective elastic thickness, and the strength of the continental lithosphere. *Geology*, *28*, 495–498.
- Mattei, M., Cifelli, F., Alimohammadian, H., Rashid, H., Winkler, A., & Sagnotti, L. (2017). Oroclinal bending in the Alborz Mountains (Northern Iran): New constraints on the age of South Caspian subduction and extrusion tectonics. *Gondwana Research*, *42*, 13–28.
- Mattei, M., Cifelli, F., Muttoni, G., & Rashid, H. (2015). Post-Cimmerian (Jurassic-Cenozoic) paleogeography and vertical axis tectonic rotations of Central Iran and the Alborz Mountains. *Journal of Asian Earth Sciences*, *102*, 92–101.
- Mattei, M., Visconti, A. L., Cifelli, F., Nozaem, R., Winkler, A., & Sagnotti, L. (2019). Clockwise paleomagnetic rotations in northeastern Iran: Major implications on recent geodynamic evolution of outer sectors of the Arabia-Eurasia collision zone. *Gondwana Research*, *71*, 194–209.
- McFadden, P. L., & McElhinny, M. W. (1990). Classification of the reversal test in aleomagnetism. *Geophysical Journal International*, *103*, 725–729.
- Ozdemir, O., & Dunlop, D. L. (1996). Thermoremanence and Neel temperature of goethite. *Geophysical Research Letters*, *23*, 921–924.
- Reilinger, R., McClusky, S., Vernant, P., Lawrence, S., Ergintav, S., Cakmak, R., et al. (2006). GPS constraints on continental deformation in the Africa-Arabia-Eurasia continental collision zone and implications for the dynamics of plate interactions. *Journal of Geophysical Research*, *111*, B05411.
- Rezaeian, M., Carter, A., Hovius, N., & Allen, M. B. (2012). Cenozoic exhumation history of the Alborz Mountains, Iran: New constraints from low-temperature chronometry. *Tectonics*, *31*, TC2004.
- Robert, A. M. M., Letouzey, J., Kavoosi, M. A., Sherkati, S., Muller, C., & Vergés, J. (2014). Structural evolution of the Kopeh Dagh fold-and-thrust belt (NE Iran) and interactions with the South Caspian Sea Basin and Amu Darya Basin. *Marine and Petroleum Geology*, *57*, 68–87.
- Ruh, J. B. (2019). Effects of fault-weakening processes on oblique intracontinental rifting and subsequent tectonic inversion. *American Journal of Science*, *319*, 315–338.
- Ruh, J. B., & Vergés, J. (2018). Effects of reactivated extensional basement faults on structural evolution of fold-and-thrust belts: Insights from numerical modelling applied to the Kopet Dagh Mountains. *Tectonophysics*, *746*, 493–511.
- Sagnotti, L., Faccenna, C., Funicello, R., & Mattei, M. (1994). Magnetic fabric and structural setting of plioleistocene clayey units in an extensional regime—the Tyrrhenian Margin of Central Italy. *Journal of Structural Geology*, *16*, 1243–1257.
- Saint-Bezar, B., Hebert, R. L., Aubourg, C., Robion, P., Swennen, R., & de Lamotte, D. F. (2002). Magnetic fabric and petrographic investigation of hematite-bearing sandstones within ramp-related folds: examples from the South Atlas Front (Morocco). *Journal of Structural Geology*, *24*, 1507–1520.
- Schwartz, S. Y., & Van der Voo, R. (1983). Paleomagnetic evaluation of the oroline hypothesis in the Central and Southern Appalachians. *Geophysical Research Letters*, *10*, 505–508.
- Shabaniyan, E., Bellier, O., Siame, L., Abbassi, M. R., Bourles, D., Braucher, R., et al. (2012). The Binalud Mountains: A key piece for the geodynamic puzzle of NE Iran. *Tectonics*, *31*(6), TC6003.
- Smith, B., Aubourg, C., Guezou, J. C., Nazari, H., Molinaro, M., Braud, X., et al. (2005). Kinematics of a sigmoidal fold and vertical axis rotation in the east of the Zagros-Makran syntaxis (southern Iran): Paleomagnetic, magnetic fabric and microtectonic approaches. *Tectonophysics*, *411*, 89–109.
- Sussman, A. J., Butler, R. F., Dinares-Turell, J., & Verges, J. (2004). Vertical-axis rotation of a foreland fold and implications for orogenic curvature: an example from the Southern Pyrenees, Spain. *Earth and Planetary Science Letters*, *218*, 435–449.
- Tan, X. D., & Kodama, K. P. (2002). Magnetic anisotropy and paleomagnetic inclination shallowing in red beds: Evidence from the Mississippian Mauch Chunk Formation. *Pennsylvania Journal of Geophysical Research*, *B11*, 2311.
- Tatavousian, S., Zoreh Bakhsh, A., Hamzeh Pour, B., Alavi Tehrani, N., Sadredini, S.E., Vaziri Tabar, F., et al. (1993). Sabzewar geological quadrangle map: 1:250,000. Geological quadrangle map of Iran No. J-4. Geological Survey of Iran, Tehran Naqshah, Tehran.
- Tavakoli, F. (2007). Present-day deformation and kinematics of the active faults observed by GPS in the Zagros and east of Iran. Geophysics [physics.geo-ph]. Université Joseph-Fourier – Grenoble I.
- Uyeda, S., Fuller, M. D., Belshe, J. C., & Girdler, R. W. (1963). Anisotropy of Magnetic Susceptibility of rocks and minerals. *Journal of Geophysical Research*, *68*, 279.
- Vernant, P., Nilforoushan, F., Hatzfeld, D., Abbassi, M. R., Vigny, C., Masson, F., et al. (2004). Present-day crustal deformation and plate kinematics in the Middle East constrained by GPS measurements in Iran and northern Oman. *Geophysical Journal International*, *157*, 381–398.
- Weil, A. B., & Yonkee, A. (2009). Anisotropy of magnetic susceptibility in weakly deformed red beds from the Wyoming salient (pp. 235–256). Sevier thrust belt: Relations to layer-parallel shortening and orogenic curvature. *Lithosphere*.

- Wilmsen, M., Fursich, F. T., Seyed-Emami, K., Majidifard, M. R., & Taheri, J. (2009). The Cimmerian Orogeny in northern Iran: tectono-stratigraphic evidence from the foreland. *Terra Nova*, 21, 211–218.
- Zanchi, A., Berra, F., Mattei, M., Ghassemi, M. R., & Sabouri, J. (2006). Inversion tectonics in central Alborz. *Iran. Journal of Structural Geology*, 28, 2023–2037.
- Zijderveld, J. D. A. (1967). A.C. demagnetization of rocks: Analysis of results. In S. K. Runcorn (Ed.), *Methods in Paleomagnetism* (pp. 254–286). Amsterdam: Elsevier.
- Zwaan, F., & Schreurs, G. (2017). *Studying scissor tectonics with 4D analogue models*. Copernicus, Vienna: EGU General Assembly.